

## LJMU Research Online

**Damiani, F, Bonito, R, Magrini, L, Prisinzano, L, Mapelli, M, Micela, G, Kalari, V, Maiz Apellaniz, J, Gilmore, G, Randich, S, Alfaro, E, Flaccomio, E, Koposov, S, Klutsch, A, Lanzafame, AC, Pancino, E, Sacco, GG, Bayo, A, Carraro, G, Casey, AR, Costado, MT, Franciosini, E, Hourihane, A, Lardo, C, Lewis, J, Monaco, L, Morbidelli, L, Worley, C, Zaggia, S, Zwitter, T and Dorda, R**

**Gaia-ESO Survey: Gas dynamics in the Carina nebula through optical emission lines**

<http://researchonline.ljmu.ac.uk/id/eprint/4844/>

### Article

**Citation** (please note it is advisable to refer to the publisher's version if you intend to cite from this work)

**Damiani, F, Bonito, R, Magrini, L, Prisinzano, L, Mapelli, M, Micela, G, Kalari, V, Maiz Apellaniz, J, Gilmore, G, Randich, S, Alfaro, E, Flaccomio, E, Koposov, S, Klutsch, A, Lanzafame, AC, Pancino, E, Sacco, GG, Bayo, A, Carraro, G. Casev. AR. Costado. MT. Franciosini. E. Hourihane. A. Lardo. C.**

LJMU has developed **LJMU Research Online** for users to access the research output of the University more effectively. Copyright © and Moral Rights for the papers on this site are retained by the individual authors and/or other copyright owners. Users may download and/or print one copy of any article(s) in LJMU Research Online to facilitate their private study or for non-commercial research. You may not engage in further distribution of the material or use it for any profit-making activities or any commercial gain.

The version presented here may differ from the published version or from the version of the record. Please see the repository URL above for details on accessing the published version and note that access may require a subscription.

For more information please contact [researchonline@ljmu.ac.uk](mailto:researchonline@ljmu.ac.uk)

# Gaia-ESO Survey: Gas dynamics in the Carina Nebula through optical emission lines. <sup>★</sup>

F. Damiani<sup>1</sup>, R. Bonito<sup>1,2</sup>, L. Magrini<sup>3</sup>, L. Prisinzano<sup>1</sup>, M. Mapelli<sup>4</sup>, G. Micela<sup>1</sup>, V. Kalari<sup>5,6</sup>, J. Maíz Apellániz<sup>7</sup>, G. Gilmore<sup>8</sup>, S. Randich<sup>3</sup>, E. Alfaro<sup>9</sup>, E. Flaccomio<sup>1</sup>, S. Koposov<sup>8,10</sup>, A. Klutsch<sup>11</sup>, A. C. Lanzafame<sup>12</sup>, E. Pancino<sup>3,13,14</sup>, G. G. Sacco<sup>3</sup>, A. Bayo<sup>15</sup>, G. Carraro<sup>16</sup>, A. R. Casey<sup>8</sup>, M. T. Costado<sup>9</sup>, E. Franciosini<sup>3</sup>, A. Hourihane<sup>8</sup>, C. Lardo<sup>17</sup>, J. Lewis<sup>8</sup>, L. Monaco<sup>18</sup>, L. Morbidelli<sup>3</sup>, C. Worley<sup>8</sup>, S. Zaggia<sup>19</sup>, T. Zwitter<sup>20</sup>, and R. Dorda<sup>21</sup>

<sup>1</sup> INAF - Osservatorio Astronomico di Palermo G.S.Vaiana, Piazza del Parlamento 1, I-90134 Palermo, Italy  
e-mail: damiani@astropa.inaf.it

<sup>2</sup> Dipartimento di Fisica e Chimica, Università di Palermo, Piazza del Parlamento 1, 90134, Palermo, Italy

<sup>3</sup> INAF - Osservatorio Astrofisico di Arcetri, Largo E. Fermi 5, 50125, Firenze, Italy

<sup>4</sup> INAF - Osservatorio Astronomico di Padova, Vicolo dell'Osservatorio 5, I-35122, Padova, Italy

<sup>5</sup> Armagh Observatory, College Hill, Armagh BT61 9DG, UK

<sup>6</sup> School of Mathematics & Physics, Queen's University Belfast, Belfast BT61 7NN, UK

<sup>7</sup> Centro de Astrobiología (CSIC-INTA), ESAC campus, Camino bajo del castillo s/n, 28 692 Villanueva de la Cañada, Madrid, Spain

<sup>8</sup> Institute of Astronomy, University of Cambridge, Madingley Road, Cambridge CB3 0HA, UK

<sup>9</sup> Instituto de Astrofísica de Andalucía-CSIC, Apdo. 3004, 18080, Granada, Spain

<sup>10</sup> Moscow MV Lomonosov State University, Sternberg Astronomical Institute, Moscow 119992, Russia

<sup>11</sup> INAF - Osservatorio Astrofisico di Catania, via S. Sofia 78, 95123, Catania, Italy

<sup>12</sup> Dipartimento di Fisica e Astronomia, Sezione Astrofisica, Università di Catania, via S. Sofia 78, 95123, Catania, Italy

<sup>13</sup> INAF - Osservatorio Astronomico di Bologna, via Ranzani 1, 40127, Bologna, Italy

<sup>14</sup> ASI Science Data Center, Via del Politecnico SNC, 00133 Roma, Italy

<sup>15</sup> Instituto de Física y Astronomía, Universidad de Valparaíso, Chile

<sup>16</sup> European Southern Observatory, Alonso de Cordova 3107 Vitacura, Santiago de Chile, Chile

<sup>17</sup> Astrophysics Research Institute, Liverpool John Moores University, 146 Brownlow Hill, Liverpool L3 5RF, UK

<sup>18</sup> Departamento de Ciencias Físicas, Universidad Andres Bello, Republica 220, Santiago, Chile

<sup>19</sup> INAF - Padova Observatory, Vicolo dell'Osservatorio 5, 35122 Padova, Italy

<sup>20</sup> Faculty of Mathematics and Physics, University of Ljubljana, Jadranska 19, 1000, Ljubljana, Slovenia

<sup>21</sup> Departamento de Física, Ingeniería de Sistemas y Teoría de la Señal, Universidad de Alicante, Apdo. 99, 03080 Alicante, Spain

Received date / Accepted date

## ABSTRACT

**Aims.** We present observations from the Gaia-ESO Survey in the lines of H $\alpha$ , [N II], [S II] and He I of nebular emission in the central part of the Carina Nebula.

**Methods.** We investigate the properties of the two already known kinematic components (approaching and receding, respectively), which account for the bulk of emission. Moreover, we investigate the features of the much less known low-intensity high-velocity (absolute RV > 50 km/s) gas emission.

**Results.** We show that gas giving rise to H $\alpha$  and He I emission is dynamically well correlated, but not identical, to gas seen through forbidden-line emission. Gas temperatures are derived from line-width ratios, and densities from [S II] doublet ratios. The spatial variation of N ionization is also studied, and found to differ between the approaching and receding components. The main result is that the bulk of the emission lines in the central part of Carina arises from several distinct shell-like expanding regions, the most evident found around  $\eta$  Car, the Trumpler 14 core, and the star WR25. Such “shells” are non-spherical, and show distortions probably caused by collisions with other shells or colder, higher-density gas. Part of them is also obscured by foreground dust lanes, while only very little dust is found in their interior. Preferential directions, parallel to the dark dust lanes, are found in the shell geometries and physical properties, probably related to strong density gradients in the studied region. We also find evidence that the ionizing flux emerging from  $\eta$  Car and the surrounding Homunculus nebula varies with polar angle. The high-velocity components in the wings of H $\alpha$  are found to arise from expanding dust reflecting the  $\eta$  Car spectrum.

**Key words.** ISM: individual objects: (Carina Nebula) – ISM: general – HII regions

## 1. Introduction

The Carina Nebula is one of the largest known star-forming complexes in the Galaxy, and has been extensively studied thanks to its relatively small distance ( $2.25 \pm 0.18$  kpc, Davidson and Humphreys 1997;  $2.35 \pm 0.5$  kpc, Smith 2006), and moderate

<sup>★</sup> Based on observations collected with the FLAMES spectrograph at VLT/UT2 telescope (Paranal Observatory, ESO, Chile), for the Gaia-ESO Large Public Survey (program 188.B-3002).

foreground reddening ( $E(B - V) = 0.36$ , Hur et al. 2012). A review of its properties is given by Smith and Brooks (2008). Several young clusters are embedded in the Nebula, most notably Trumpler 14 and 16, and Collinder 228, which all together form the Car OB1 association. This is one of the largest OB associations in the Galaxy, with more than 60 stars earlier than B0, and several WR stars. The most studied member of Trumpler 16 is the luminous blue variable (LBV)  $\eta$  Car. About one-third of all known O3 stars in the Galaxy, and the first discovered O2 star, are found in Trumpler 14 and 16.

The age of the Carina star-forming region (SFR) and its component clusters has been estimated in the range from 1 to several Myr. Wolk et al. (2011) remarks however that no simple age sequence is able to explain the respective properties of clusters Trumpler 14, 15, and 16, so that other parameters come into play to define the properties of these regions. There are also hints of a past supernova explosion in the region (see Smith and Brooks 2008, Townsley et al. 2011). The region is still actively forming stars in its outer parts (Smith et al. 2000; Smith, Bally and Brooks 2004; Smith, Stassun and Bally 2005; Povich et al. 2011), and shows many dense dusty patches (“pillars”), seen against the very bright emission from the  $H_{II}$  region. Extinction within the molecular cloud, where Carina star clusters are still partially embedded, spans a wide range (up to  $A_V \sim 15$  among X-ray detected 2MASS sources, and perhaps more, Albacete-Colombo et al. 2008), hiding most background stars from optical observations in the central parts of the clusters.

The stellar population in the Carina SFR was recently observed as part of the Gaia-ESO spectroscopic Survey, which will cover more than  $10^5$  stars belonging to all components of the Milky Way, including some very young clusters (Gilmore et al. 2012, Randich et al. 2013). More than 1000 low-mass stars, and several hundreds OB stars, have been observed towards Carina, using the ESO VLT/FLAMES multi-fibre spectrograph (Pasquini et al. 2002). This allows simultaneous observations of  $\sim 130$  targets (stars and sky positions) at intermediate resolution ( $R \sim 15000 - 20000$ , depending on setup) with the Giraffe spectrograph, and 7-8 positions at high resolution with the UVES spectrograph. Several fibres per Observing Block (OB; each OB comprises all spectra recorded simultaneously) were aimed at “empty” sky positions, to estimate the sky contribution expected in stellar spectra. Therefore, the Survey data contain a rich dataset of pure sky spectra, at positions scattered across the Nebula, containing an amount of information on the ionized component of the diffuse medium towards that line of sight, which we study in this work. The spectra of low-mass stars in the field will be studied in a later work (Damiani et al., in preparation).

The diffuse medium in Carina is already known to be complex, and contains a mixture of components across a huge range of temperatures. For example, cold gas was imaged in CO lines by Yonekura et al. (2005); intermediate-temperature gas emitting in the optical lines was studied by Deharveng and Maucherat (1975), Walborn and Hesser (1975), Meaburn, Lopez and Keir (1984); the whole Nebula was found to be permeated by million-degree hot gas by Seward et al. (1979) and Townsley et al. (2011). Smith and Brooks (2007) made a comparative review of large-scale observations of its diffuse medium.

In this paper, we focus on the analysis of pure sky spectra in the central part of the Carina nebula, obtained by the Gaia-ESO survey. In particular, we focus on the kinematic properties of  $H\alpha$ , [NII], [SII] and He I nebular emission lines. In Section 2 we describe the observations, while in Section 3 we present our results. In Section 4 we discuss the main implications of our work

for the dynamics of gas in the Carina nebula, while Section 5 summarizes our conclusions.

## 2. Observational data

The spectra used in this work were obtained mostly with the Giraffe HR15N setup ( $R \sim 19000$ ), in the wavelength range 6444-6818Å. Thirteen OBs were executed using this setup in Carina, yielding 185 sky spectra, at 137 individual sky positions (35 sky positions were observed more than once). Using Giraffe setup HR14A, 114 sky spectra are also available, in the wavelength range 6301-6689Å ( $R \sim 18000$ ), overlapping that of setup HR15N<sup>1</sup>. Moreover, 15 sky spectra were also obtained with UVES (580nm setup,  $R \sim 47000$ ), in the ranges 4768-5802Å (lower arm), and 5822-6831Å (upper arm). The Survey targets are low-mass stars ranging down to magnitude  $V \sim 18.5$ : for about half of the 1085 stars observed with setup HR15N, the sky brightness at  $H\alpha$  (as recorded by the 1.2-arcsec-wide Giraffe fibres) is 100-1000 times the stellar continuum, so that high-quality information on the sky emission, at least in the  $H\alpha$  core, was obtained also from the spectra of these faint stars<sup>2</sup>. In total, we have some information for more than 650 sky positions across the Nebula. All spectra presented here are from internal data release *GESiDR4*.

Figure 1 shows a DSS image of the Nebula, with indicated the sky positions studied here. The bright diffuse emission is bounded towards South by a ‘V’ shaped dust obscuration.  $\eta$  Car is the brightest star, a few arcmin East from image center, and the cluster Trumpler 16 is found all around it, projected against the brightest part of the Nebula. To the North-west is visible the compact, massive cluster Trumpler 14 (Tr 14). Just West of  $\eta$  Car, the obscured region with a peculiar shape is the so-called ‘Keyhole’ nebula, already described by John Herschel. As the Figure shows, our observations cover widely different regions of the Nebula.

The HR15N wavelength range contains several important nebular lines:  $H\alpha$ , the neighboring [N II] lines at 6548, 6584Å, the He I line at 6678Å, and the two [S II] lines at 6716, 6731Å. The HR14A range contains the same lines except for the [S II] lines. UVES spectra, in addition to these (and many other) lines, also allow the study of  $H\beta$ .

## 3. Results

An example of HR15N sky spectrum is shown in Figure 2. From a close inspection, it is seen that most line profiles show double peaks, as shown in the examples of Figure 3. This is not a new discovery, since it was already noted by several authors (Deharveng and Maucherat 1975; Walborn and Hesser 1975; Meaburn, Lopez and Keir 1984), but the spectral resolution and signal-to-noise ratio (S/N) offered by our new data permit a deeper study of the phenomenon. Figure 3 illustrates conveniently the wide range of emission line profiles found in the Nebula: in  $H\alpha$  (red curves), only panels *b*, *c*, and *d* show a distinct double-peak

<sup>1</sup> All targets observed using setup HR14A were also observed with Giraffe setups HR3 (4033-4201 Å), HR5A (4340-4587 Å), and HR6 (4538-4759 Å), which however do not show strong nebular lines and are therefore not considered here.

<sup>2</sup> The typical peak  $H\alpha$  brightness in classical T Tauri stars rarely (if ever) exceeds 10 times the star continuum level, see e.g. Cohen and Kuhi (1979). Moreover, most member stars in Carina are expected to be weak-line T Tauri from their weak near-IR excesses (Albacete-Colombo et al. 2008), and therefore have still weaker  $H\alpha$  emission.

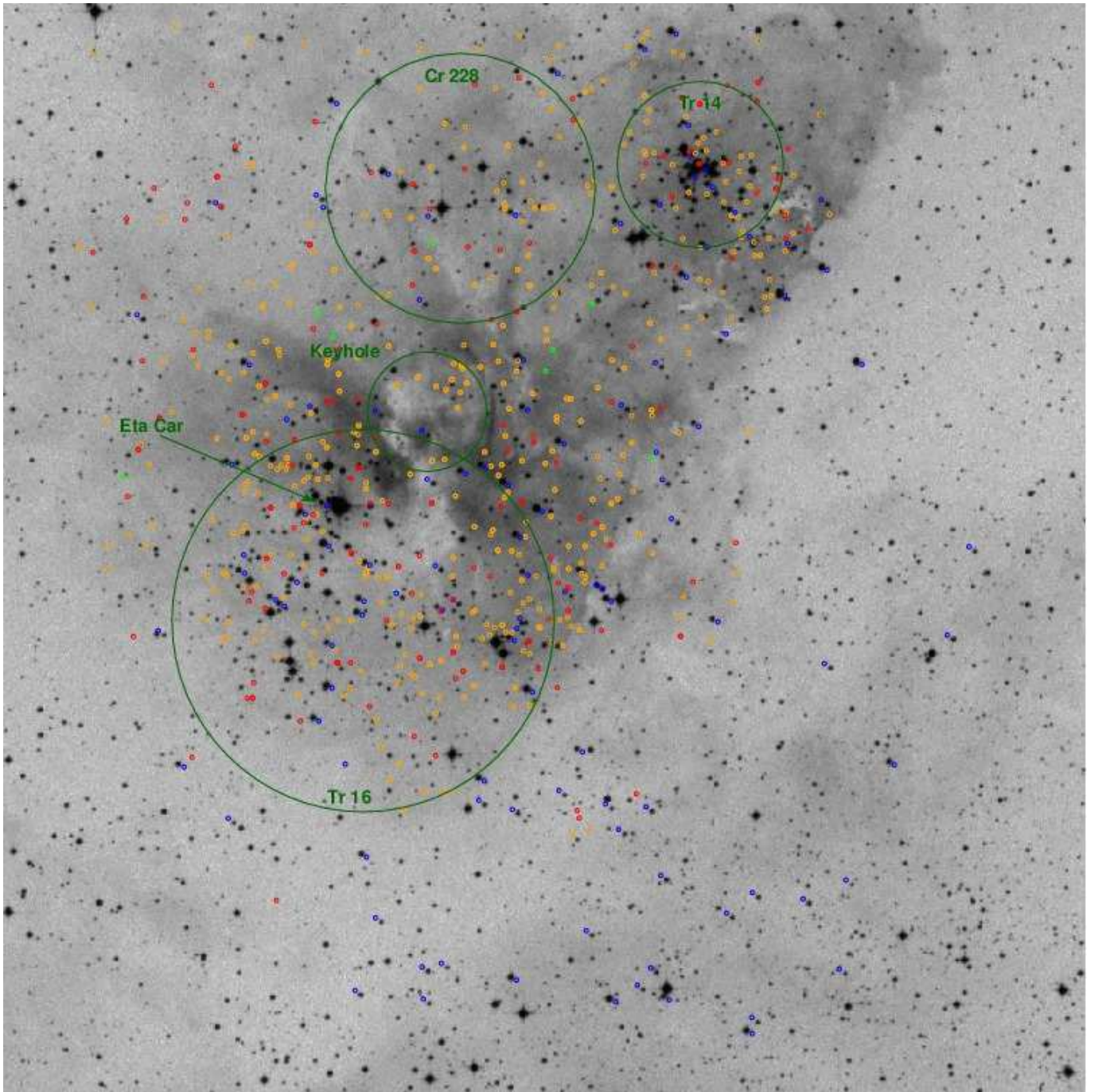


**Fig. 1.** DSS1 image of the central part of the Carina Nebula, of size  $26' \times 26'$ , corresponding to 17.4 pc on a side at the Nebula distance of 2.3 kpc. North is up and East is to the left. Red circles indicate positions of sky fibres, using Giraffe setup HR15N. Orange circles indicate fibres on faint stars with HR15N. Blue circles are sky fibres using setup HR14A, and light-green circles are UVES sky fibres. Big dark-green circles indicate the approximate positions of clusters studied here, and the Keyhole nebula. The dark-green arrow indicates the star  $\eta$  Car.

structure; panels *a* and *f* show asymmetries in the line, while a superficial look at panel *e* does not reveal more than a single gaussian component. In the latter line profiles of panels *a*, *f* and *e*, however, two components are clearly seen in the He I (magenta) and [N II] lines (blue and black). Looking at the radial velocity (RV) of the line peaks we observe an approximate correspondence between the peaks of the different lines. As panels *b*, *c*, and *f* show clearly, there is instead no correlation between the intensities of  $H\alpha$  and the corresponding peak in the [N II] line. On the contrary, the intensities of the He I peaks show a nearly perfect correspondence with those of  $H\alpha$ .

We have fitted all the  $H\alpha$ , [N II] 6584Å, and He I line profiles using two gaussians; we have not attempted the same fit on the [N II] 6548Å line, since this is weaker by a constant factor 2.95 (set by atomic physics) than the [N II] 6584Å line. The best-fit functions are also shown in Fig. 3 with orange ( $H\alpha$ ), cyan ([N II]) and purple (He I) colors: the fit to  $H\alpha$  is extremely good, being almost indistinguishable from the observed line profile; even in the case of distorted, single-peak profiles (e.g., panel *e*) two gaussian components are actually required to yield a good fit. There are very few cases where the  $H\alpha$  profiles seemed to require a third component, or even a single component was sufficient: in



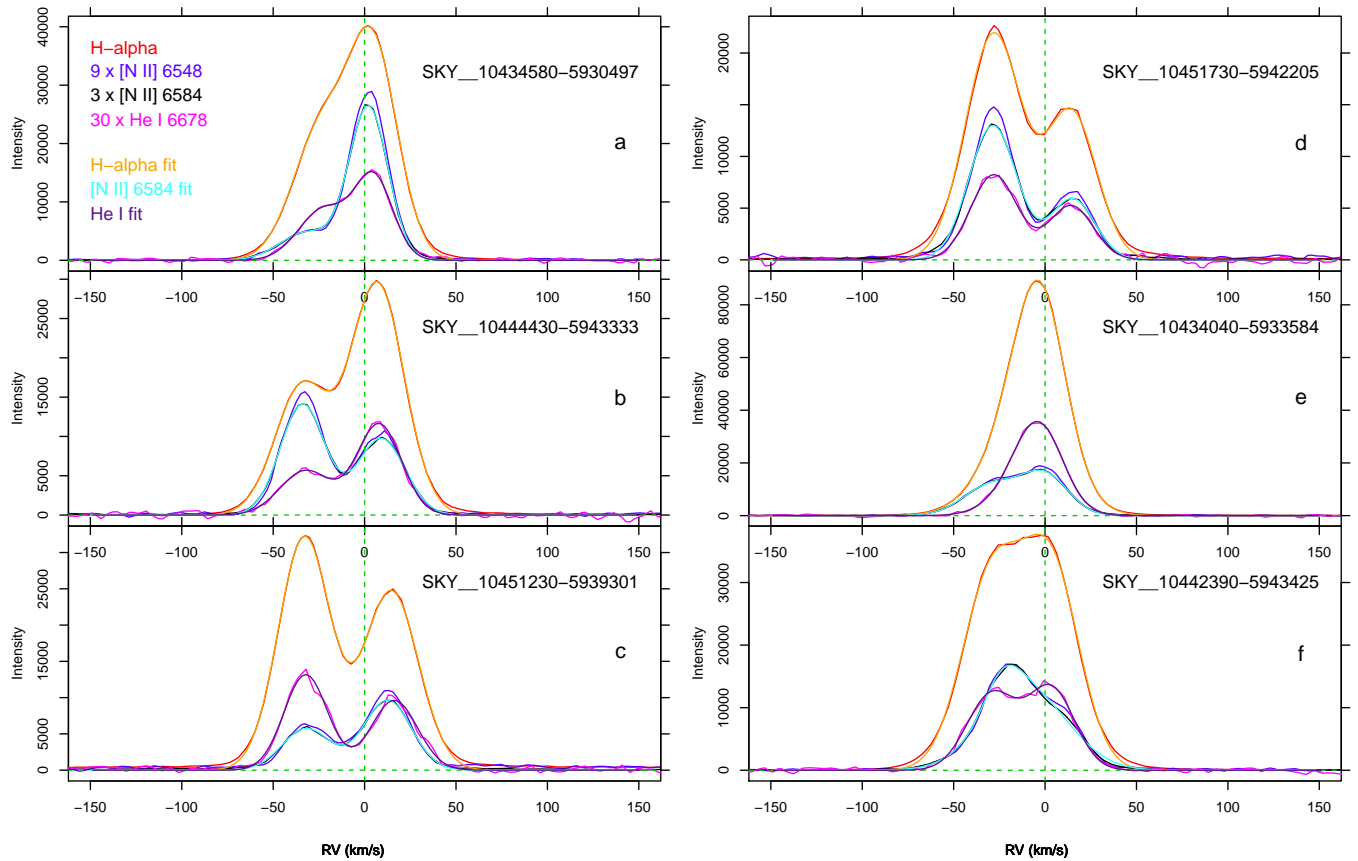


**Fig. 3.** Examples of line profiles at  $H\alpha$  (red), [N II] 6548 (blue) and 6584Å (black), and He I (magenta), for various positions across the Nebula. Also shown are two-gaussian best fits for  $H\alpha$  (orange), [N II] 6584Å (cyan), and He I (purple). Note that the lines shown are scaled by the indicated factors, for ease of comparison with  $H\alpha$ . Indicated radial velocities are heliocentric.

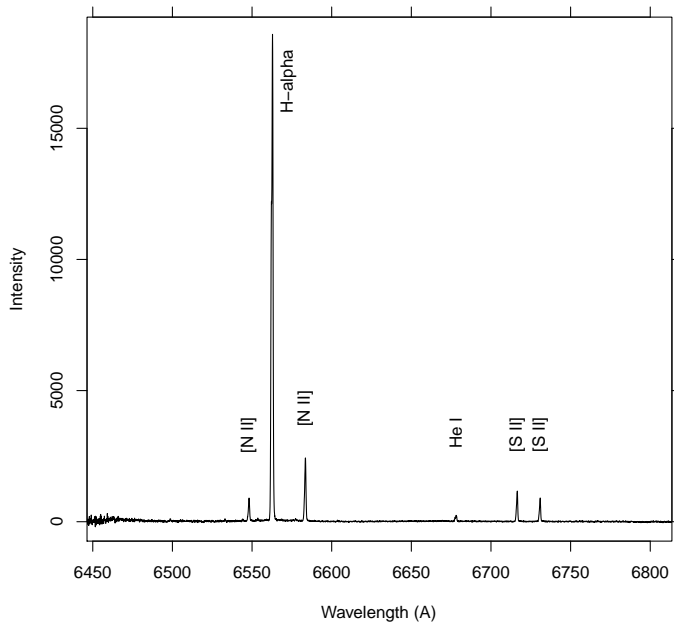


**Fig. 2.** Example of typical sky spectrum in Carina, obtained with the Giraffe HR15N setup. Prominent nebular lines are labelled.

the vast majority of cases two gaussians are required. The [N II] and He I lines are also equally well fitted by two-gaussian models, although in these cases the agreement is limited by the

lower S/N of the lines (especially He I). We present in Tables 1, 2, and 3 all best-fit parameters of the two-gaussian models for  $H\alpha$ , [N II] 6584Å, He I, and also [S II] 6717 and 6731Å lines<sup>3</sup>. In Table 1, column *Type/setup* indicates the origin of spectrum (sky fibre or faint star), and the Giraffe setup used; columns *RV* and  $\sigma$  are in units of km/s.

The persistent two components across the whole set of line profiles in the Nebula (analogous fits were performed on sky-dominated stellar spectra, and on HR14A spectra, with similar results) suggests the existence of two well-defined, distinct dynamical components. Since the gaussian fits represent so faithfully the observed line profiles, we examine the properties of the two components using the best-fit parameter values. This allows to study the bulk of nebular emission in Carina, and will be done in the next Section. A very careful inspection of Fig. 3, however, shows that in the far wings of  $H\alpha$  the two-gaussian fit differs from the observed profiles: these residual emissions are found to possess interesting characteristics, and will be studied in Section 3.2.

### 3.1. Main components

From here on, we will refer to the bluer component of the lines as the 'approaching' component, and to the redder one as 'receding', in a relative sense since they may both happen to have a

<sup>3</sup> Each gaussian component will have the analytical form  $(Norm/\sqrt{2\pi\sigma^2})\exp(-(rv - RV)^2/2\sigma^2)$  using the tabulated parameters.

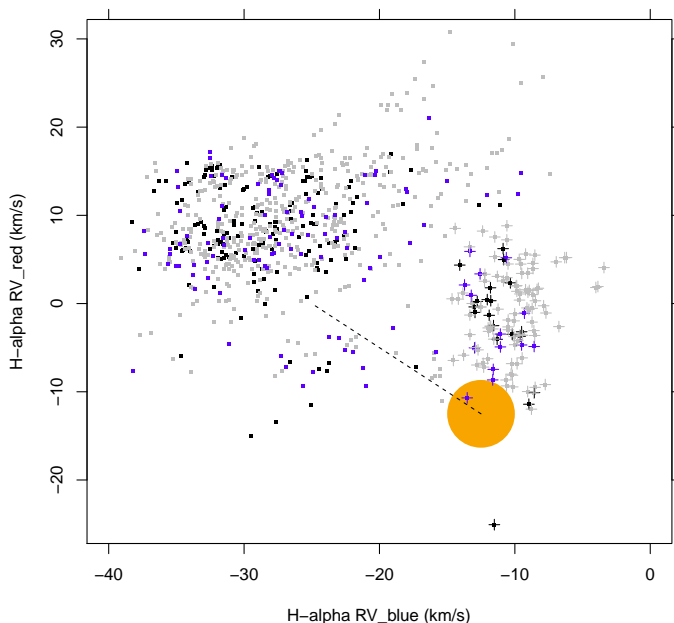


**Fig. 4.** Radial velocity of the receding component vs. RV of the approaching component. Here black dots refer to pure-sky fibres from HR15N setup, blue dots to pure-sky from HR14A setup, while grey dots to sky lines from faint stars. The orange circles represent the average RV of low-mass cluster stars. The dashed line is the expected locus for purely spherical expansion. A subsample of apparently peculiar datapoints is highlighted using '+' symbols.

positive (or negative) RV on the same sightline. As the sky image of Fig. 1 shows, the bright nebulousity is centered on the cluster Trumpler 16, so it can be expected that its dynamics is related to the cluster dynamics. Wilson (1953) reports for  $\eta$  Car a RV of -25 km/s. We anticipate here that bona-fide low-mass members of Trumpler 16, from the same Gaia-ESO HR15N dataset studied here, have RVs in the range of -10 to -15 km/s (Damiani et al., in preparation), and the low-mass star RVs are usually more accurate than those from massive stars, because these latter have fewer and broader lines. We assume therefore a 'fiducial' RV for the Trumpler 16-14 clusters of -12.5 km/s; in our preliminary analysis, no difference in mean RV is found between clusters Trumpler 16 and 14.

Figure 4 shows the best-fit RVs of the receding H $\alpha$  component  $RV_{red}$  vs. that of the approaching H $\alpha$  component  $RV_{blue}$ . Datapoints refer to pure-sky HR15N data (black), sky from faint stars (grey), and pure-sky HR14A data (blue). The orange circle describes the locus of cluster stars, i.e., the center-of-mass velocity of the cluster  $RV_{cm}$  (Damiani et al., in preparation). It can be seen that datapoints split naturally in two main groups (equally populated by black, grey and blue dots): a larger group centered at  $(RV_{blue}, RV_{red}) = (-30, 10)$ , and a smaller one, closer to  $RV_{cm}$ . We have indicated these latter observations (at  $RV_{blue} > -15$  and  $RV_{red} < 10$ ) with small plus signs, and we will refer to these sky locations as "zero-velocity gas" (with respect to  $RV_{cm}$ ). Note that even for zero-velocity datapoints we are still able to fit two distinct, non-degenerate gaussian components to most lines, thanks to the very large signal-to-noise ratio of our spectra. The dashed line starting at  $RV_{cm}$  is the expected locus for an ideal, spherical, optically thin expanding region, whatever its geometrical thickness or velocity law. The requirement of symmetry, in fact, makes that for each line of sight towards it two RV values are observed, symmetrically on opposite sides of  $RV_{cm}$  (i.e.,

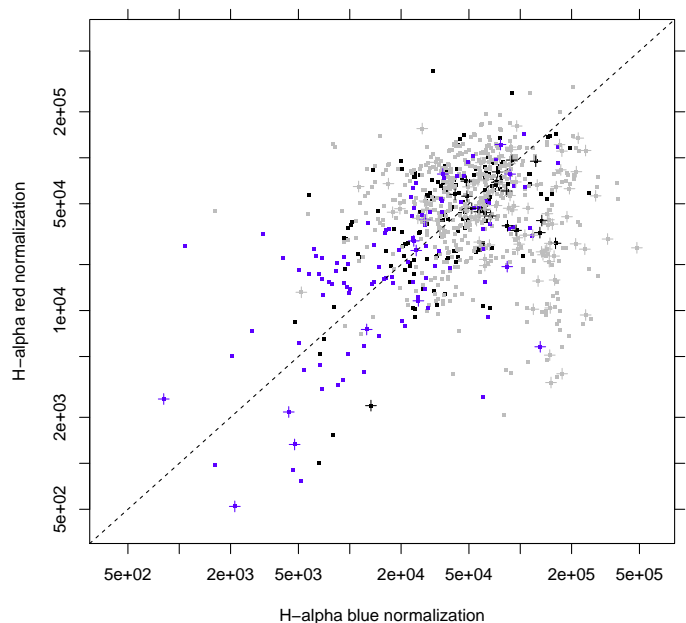


**Fig. 5.** Normalizations of best-fit gaussians for the receding vs. approaching components. The dashed line represents identity. Other symbols as in Fig. 4.

the velocity of the center of expansion). This behaviour is actually shown by planetary nebulae (Osterbrock and Ferland 2006). Fig. 4 shows instead that no global spherical expansion occurs in the studied part of the Carina Nebula, and there is no one-to-one correspondence between  $RV_{blue}$  and  $RV_{red}$  on the same line of sight. Only the average approaching and receding RVs of the main group of datapoints are found on the prolongement of the dashed segment: on average, the approaching and receding RVs are respectively equal to  $RV_{cm} - 20$  and  $RV_{cm} + 20$  km/s, but no well-defined center of expansion is identifiable in the data.

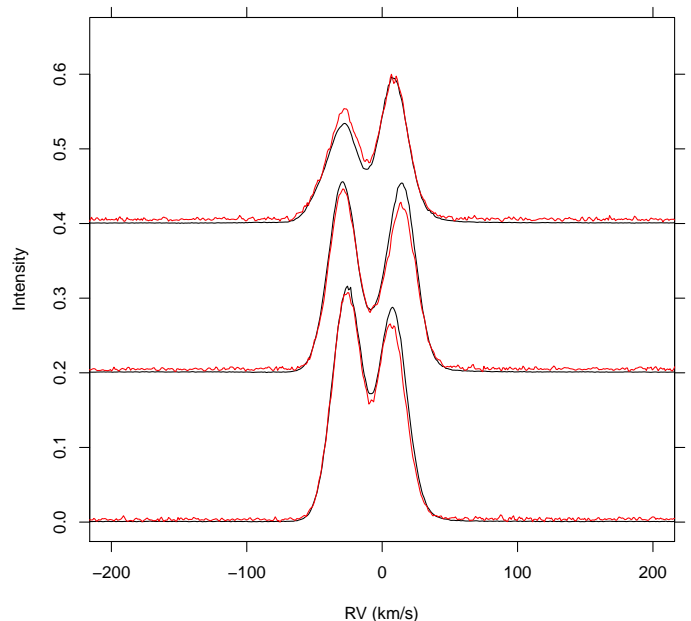
Since the datapoints are not smoothly connected to the center-of-mass velocity, the approaching and receding components resemble more two distinct layers of gas than a spherical distribution; alternatively, the distribution might still be spherical, but our observations only cover its central parts, and omit parts where expansion is orthogonal to the line of sight, and thus at  $RV \sim 0$ . Smith and Brooks (2007) discuss the large-scale diffuse emission in Carina, made of several shell-like features roughly centered on Trumpler 14-16 of sizes 20-30 pc, and suggest that the double-peaked optical lines would arise from opposite sides of those shells, along the line of sight. This hypothesis, however, fails to explain why the intensity of the H $\alpha$  emission is so spatially concentrated near the central clusters, at intensities much larger than the outer border of the shells, while projection effects would cause the reverse effect (largest dilution at the center). The line-of-sight depth of the regions producing the most intense H $\alpha$  emission can be expected to be of order of its sky-projected size, or  $\sim 10$  pc in diameter. This might be a sufficiently large size to account for the lack of precise correspondence between  $RV_{blue}$  and  $RV_{red}$  along the same line of sight. We must not forget, nevertheless, the known complexity of the Carina SFR, and the possibility that there are actually several distinct centers of expansion, perhaps at different RVs. The observed emission might therefore be a chaotic superposition of different expanding spheres.

Figure 5 shows the intensity of  $H\alpha$  of the approaching component vs. that of the receding component. Only a weak correlation exists between the two, dominated by the datapoints (blue dots) from the HR14A dataset, coming partly from stars outside the strong nebulosity, to the South-west. The intensity pattern in the receding component is therefore sensibly different in its morphological details than that of the approaching component, a result that  $H\alpha$  images might have never shown. The zero-velocity gas already defined in Fig. 4 is also indicated in Fig. 5 with small plus signs. We also observe that the intensity of the  $H\alpha$  lines from the receding and approaching gas are on average similar: if they have intrinsically similar brightnesses, then the absorption towards them cannot be sensibly different (much less than one magnitude of extinction), and only a low amount of dust may exist between them, despite the large distance which is likely to separate them.

Thus far we have assumed implicitly that the receding gas is generated from expansion starting from some place inside clusters Trumpler 16 and 14, and is located at larger distances than the clusters themselves, while the opposite holds for the blue-shifted, approaching gas. In principle, it would not be impossible to have the reversed situation, where the two layers are actually moving towards one another, leading to a huge collision, which might have already generated the existing massive clusters. In order to discriminate between the two scenarios, it is necessary to determine unambiguously which layer is closer to us. We have seen that extinction differences, if they exist, are subtle, and cannot be determined from the statistical arguments discussed above. However, a much more accurate way to establish the reddening suffered by optical line emission is through the Balmer decrement. For this aim we use the 15 UVES pure-sky spectra, which include both  $H\alpha$  and  $H\beta$ . Being no spectrophotometric instrument, we cannot determine absolute reddenings for the two layers (i.e., calibrated flux ratios between  $H\alpha$  and  $H\beta$ ); however, it is possible to find which layer has the largest reddening of the two. Figure 6 shows examples of comparison between  $H\alpha$  (black) and  $H\beta$  (red): in all cases the receding, red-shifted layer shows slightly attenuated  $H\beta$  intensity with respect to  $H\alpha$ , and thus larger reddening. The reverse is never found. This may be taken as evidence that the two layers are expanding away from the central clusters and  $\eta$  Car, although a different temperature between the two layers might mimic the same effect (Osterbrock and Ferland 2006).

We have compared best-fit parameters between different lines, starting from  $H\alpha$  and He I. The respective RVs are shown in Figure 7, where red (blue) dots indicate the receding (approaching) components from HR15N data, and pink (purple) dots the same components from HR14A data, respectively. The agreement is excellent, except for a few outliers, most of which already known as the “zero-velocity” gas (plus signs). It should be noted that the He I line is by far the weakest line in our sample (Fig. 2), with intensity  $\sim 1/90$  of  $H\alpha$ , so that in Fig. 7 errors in the ordinates must be much larger than errors in the abscissae; the latter are expected to be of the same size as the plotted dots. The very good coincidence in RVs suggests strongly that the same gas is emitting in these two lines. This conclusion is reinforced by the comparison of the intensities in the two lines in Figure 8, which shows again a very tight correlation.

Since the same material emits in  $H\alpha$  and He I lines, the slight difference in their line widths, already observed with reference to Fig. 3 above, must be related to microscopic properties of the gas, and can be taken as a measure of temperature. The total line



**Fig. 6.** Examples of  $H\beta$  (red) and  $H\alpha$  (black) lines from pure-sky fibres using UVES. A vertical shift was applied to spectra from different sky positions.  $H\beta$  lines were scaled up by a factor of 7.

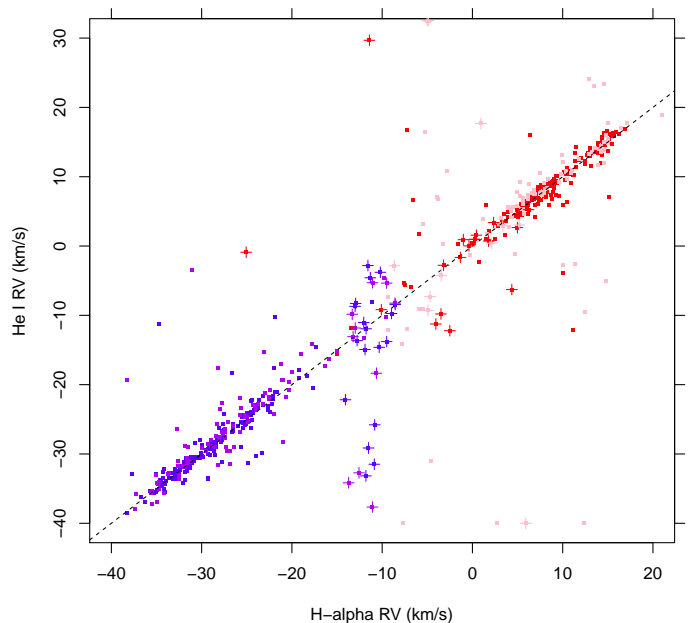


**Fig. 7.** Radial velocity from the He I 6678 Å line vs. RV from  $H\alpha$ . Red (blue) symbols refer to the receding (approaching) component from HR15N data. Purple (pink) symbols refer to the same two components, but from HR14A pure-sky fibres. Plus symbols refer to “zero-velocity” gas as in previous Figures. The dashed line represents identity.

width for hydrogen will be:

$$\sigma_H = \sqrt{\sigma_T^2 + kT/m_H} \quad (1)$$

and an analogous expression, with the appropriate atomic mass, for He.  $\sigma_T$  is the component of the line width due to instrumental width and turbulence (and any other macroscopic velocity field, identical for hydrogen and helium, and therefore irrelevant for



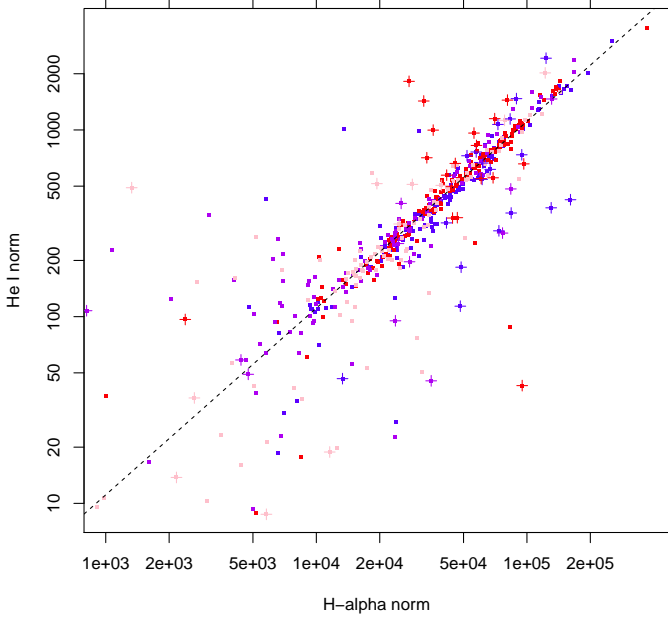


**Fig. 8.** Fit normalization for He I vs. normalization for H $\alpha$ . Symbols as in Fig. 7. The dashed line indicates a constant ratio of 1/90.

our derivation of temperature). Therefore, we plot in Figure 9 the H $\alpha$  and He I line widths, with three loci of constant temperature (5000, 10000, 15000 K). Most datapoints fall between 5000-15000 K; strong outliers are more likely to arise from failed fits than from extremely high (low) temperatures. Datapoints for the approaching (blue) gas tend to show larger temperatures than those of receding gas, by a few thousands K. Turbulent velocities span a range of approximately 7-15 km/s (net of the instrumental line width), often above the sound speed for  $T \sim 10000$  K.

Next, we have compared H $\alpha$  parameters with those for [N II] 6584Å (the strongest of the [N II] doublet). The RV comparison is shown in Figure 10: the agreement between the respective RVs is much worse than in the case of He I of Fig. 7. The [N II] line is about 20 times stronger than the He I line, so the disagreement is certainly not due to errors, but is real, and a definite indication that the gas emitting H $\alpha$  is not strictly the same as that emitting the [N II] lines. Although not the same gas, the dynamics of these two components is similar, since the H $\alpha$  and [N II] RVs are nevertheless well correlated (the receding gas more so than the approaching gas): they might be two adjacent layers or bubbles in the same expanding material. We note that there is no definite sense in which the respective RVs differ: if for example the H $\alpha$ -emitting gas were moving systematically faster than the [N II]-emitting gas, one would observe a correlation with a slope different from 1 (the dashed line), still centered on  $RV_{cm}$ . The “zero-velocity” outliers (plus signs) are found in [N II] sometimes at  $RV \sim RV_{cm}$ , and sometimes at definite non-zero RV. We will return to this point below.

The comparison between the intensities of H $\alpha$  and [N II] strenghtens the conclusion that they arise from different material even more (Figure 11), with intensity ratios between the two lines spanning an order of magnitude (or more). We will discuss below the interpretation of this fact.

The comparison between the RVs from H $\alpha$  with those from the [S II] 6717Å line is shown in Figure 12. Here, many more datapoints are shown than in Fig. 10, from observations of sky lines from faint-star HR15N spectra. On the other hand, data-

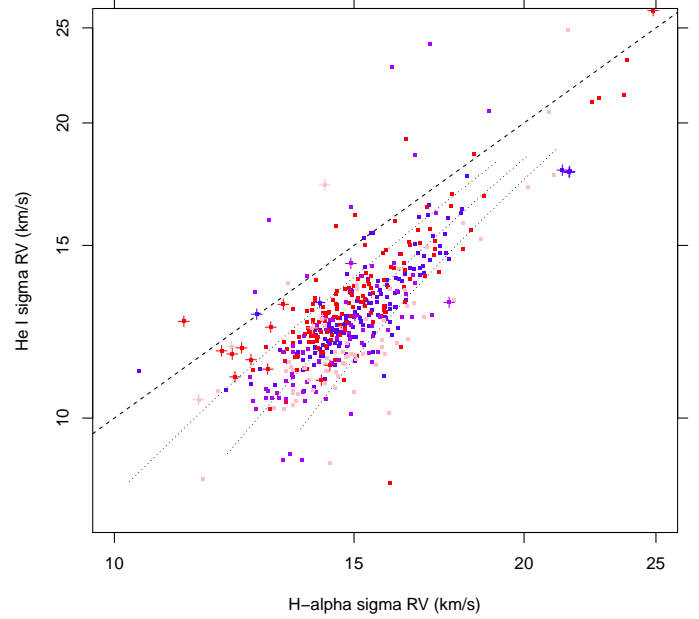


**Fig. 9.** Gaussian widths  $\sigma$  of He I lines vs. those of H $\alpha$ . The three dotted lines represent loci of constant gas temperature,  $T_{gas} = 5000, 10000, 15000$  K from top to bottom. The dashed line represents equality. Symbols as in Fig. 7. Only datapoints with the same RV from H $\alpha$  and He I within 3 km/s are shown.

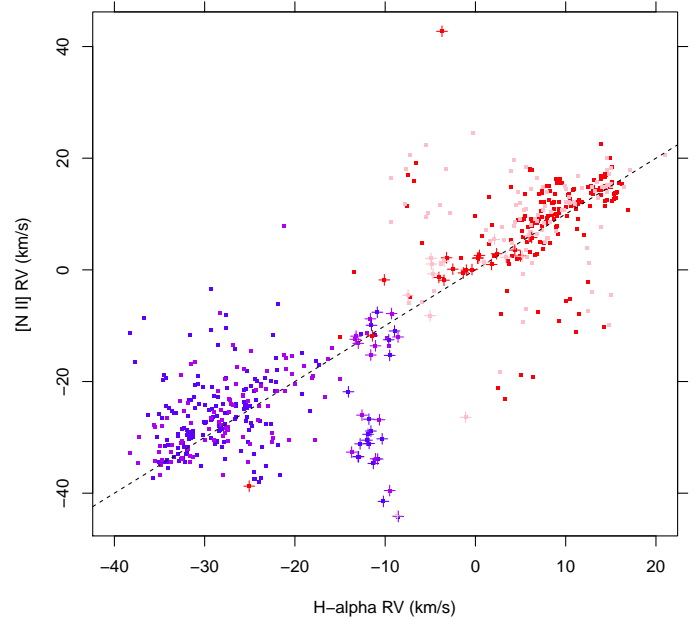


**Fig. 10.** Radial velocity from the [N II] 6584 Å line vs. RV from H $\alpha$ . Symbols as in Fig. 7.

points from HR14A observations are missing since the [S II] lines are outside their wavelength range. Fig. 12 shows the same pattern as Fig. 10, with a loose correlation and a peculiar place for the zero-velocity gas. This suggests at least a similarity in the dynamics of the [S II]-emitting and [N II]-emitting gas, which is confirmed by their direct comparison, shown in Figure 13. Despite the fact that both lines are stronger than He I, the latter correlation is not as tight as that between H $\alpha$  and He I, so that

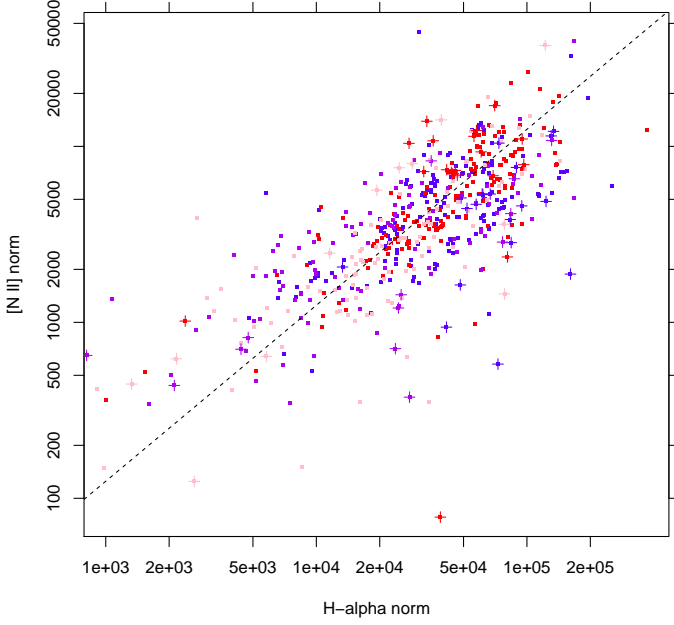


**Fig. 11.** Fit normalization for [N II] vs. normalization for H $\alpha$ . The dashed line indicates a constant ratio of 1/8. Other symbols as in Fig. 10.

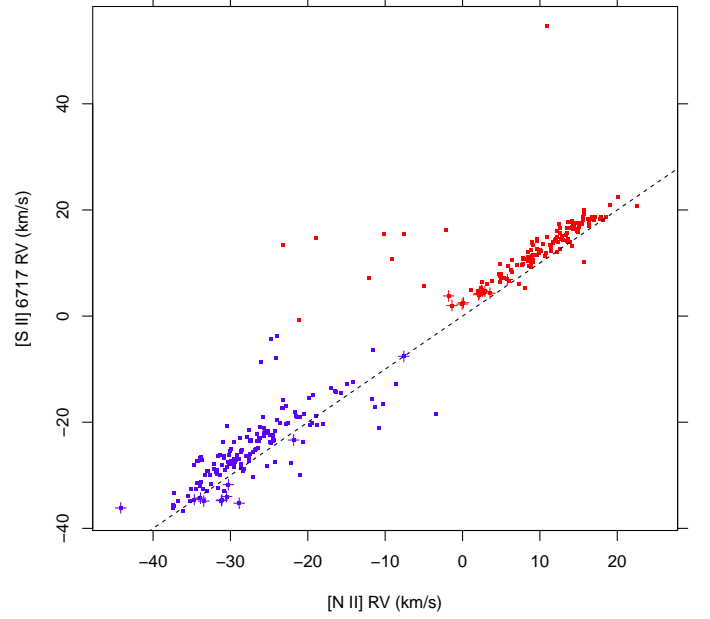


**Fig. 13.** Radial velocity from the [S II] 6717 Å line vs. RV from [N II] 6584 Å. Symbols as in Fig. 7.

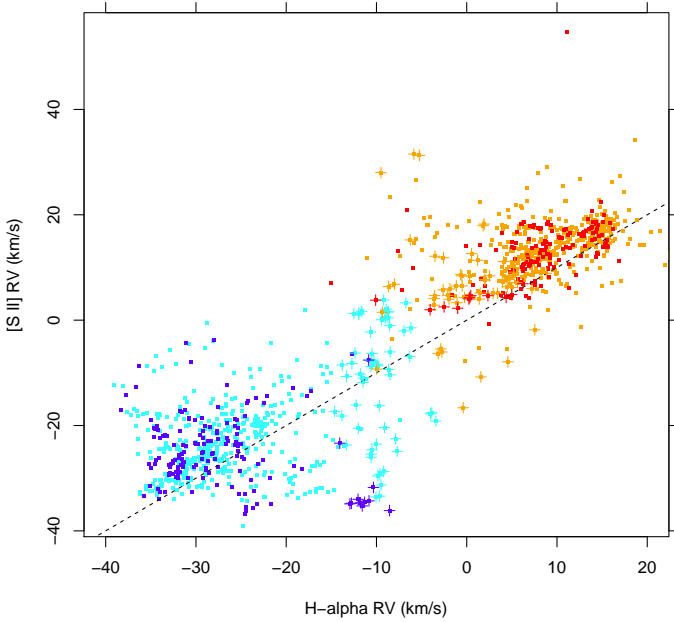


**Fig. 12.** Radial velocity from the [S II] 6717 Å line vs. RV from H $\alpha$ . Red (blue) symbols refer to the receding (approaching) component from HR15N data. Cyan (orange) symbols refer to the same two components, but from HR15N observations of faint stars. Other symbols as in Fig. 7.

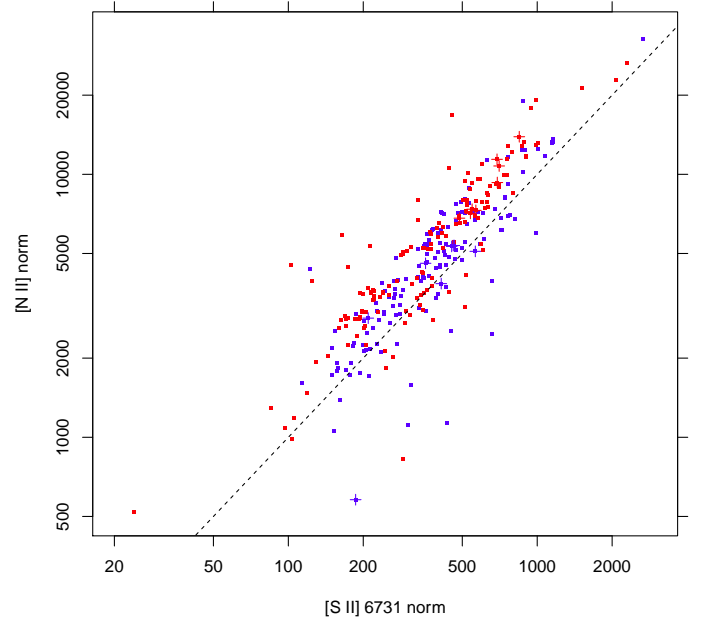


**Fig. 14.** Fit normalization of [N II] 6584 Å vs. [S II] 6731 Å. Symbols as in Fig. 7.

again the conclusion is that the [S II]-emitting gas is nearly coincident, but not identical, to the [N II]-emitting gas. In Fig. 13 we also note that most of zero-velocity datapoints are not outliers here, but follow the same correlation as other datapoints. Since the plotted data are statistically independent, this demonstrates that those points do not arise from failed fits, but have a real significance. The same considerations apply to the compar-

ison between [S II] and [N II] intensities in Figure 14: a good correlation, but significantly different from identity.

Following this preliminary assessment, we have examined the ratio between the two [S II] 6717/6731 Å lines, which depends only on the gas density, for densities in the range  $10^2 - 10^5 \text{ cm}^{-3}$  (Osterbrock and Ferland 2006). A plot of the ratio between the H $\alpha$  and He I line widths (a proxy for temperature as discussed above) vs. the [S II] 6717/6731 Å intensity ratio is shown in Figure 15. There is a tendency for the approaching gas to have both higher temperatures and lower densities (higher 6717/6731 Å ratio) than the receding gas; median 6717/6731 Å

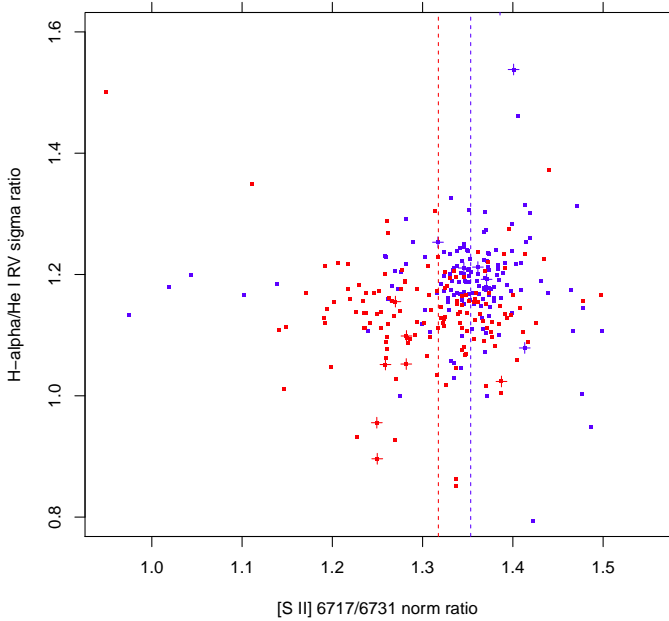


**Fig. 15.** Gaussian width ratio between H $\alpha$  and He I (proxy for temperature), vs. normalization ratio between [S II] 6717/6731 Å (proxy for density). Temperature increases upwards, while density increases towards the left. Symbols are as in Fig. 7. The red (blue) vertical dashed line indicates the median [S II] 6717/6731 Å ratio for the receding (approaching) components. On average, the receding component has higher density and lower temperature than the approaching component.

ratios are indicated by the vertical dashed lines, and correspond to densities of  $100 (\times \sqrt{10^4/T}) \text{ cm}^{-3}$ , and  $200 (\times \sqrt{10^4/T}) \text{ cm}^{-3}$ , respectively.

A plot of the [S II] 6717/6731 Å intensity ratio vs. intensity of the [S II] 6731 Å line is instead shown in Figure 16. The correlation, although not strict, indicates that for increasingly strong [S II] emission the density of the emitting gas also increases, with the largest electron densities found being  $\sim 2 \times 10^3 (\times \sqrt{10^4/T}) \text{ cm}^{-3}$ .

### 3.2. Low intensity components

The two emission components well described by gaussian shapes constitute the bulk of the nebular emission in the studied region. However, as anticipated from close inspection of Fig. 3, there are small but significant departures from these pure gaussian shapes in their extreme wings. We are able to study these low-intensity wings thanks to the very high S/N of our data. To this purpose we consider spectra from sky fibers only, to avoid any possibility of confusion with stellar features. After subtracting out the best-fit gaussian components from the lines, residual emission can in most cases be seen, of which representative examples are shown in Figure 17. The intensity levels of this emission are about two orders of magnitude lower than the peak H $\alpha$  emission. Figure 17 shows residuals in H $\alpha$  (orange), He I 6678 (green), and the [S II] lines (6717 Å in blue, and 6731 Å in red). The two black dashed lines indicate the best-fit RVs of the main gaussian approaching/receding components. The grey dashed lines indicate RVs of  $RV_{cm} \pm (50, 100, 380) \text{ km/s}$ , for ref-

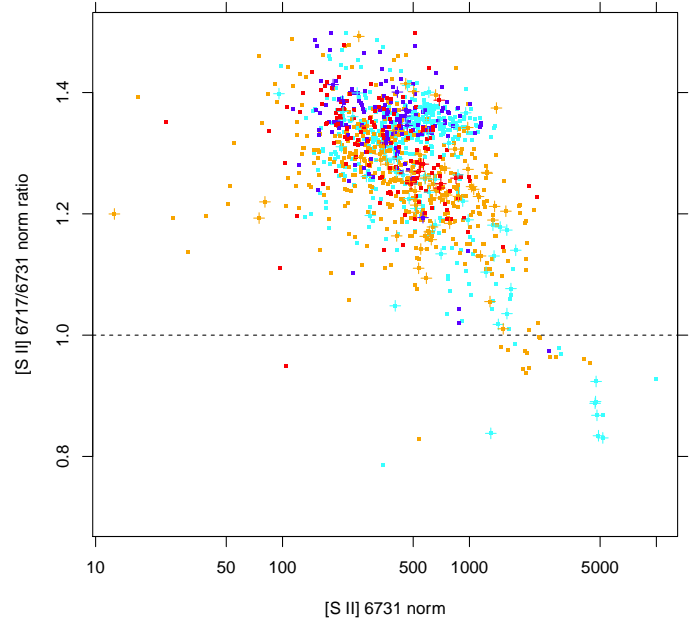


**Fig. 16.** Intensity ratio between [S II] 6717 Å and 6731 Å lines, vs. intensity of [S II] 6731 Å. Symbols as in Fig. 12. The dashed line at unity ratio corresponds to electron density  $N_e \sim 600 \text{ cm}^{-3}$ .

erence<sup>4</sup>. We demonstrate in the Appendix that the residual patterns seen in Fig. 17 are not of instrumental origin. First, we note from the Figure that the residual emission in H $\alpha$  shows two apparently distinct components: a lower-intensity high-velocity gas, with RV reaching (absolute) values up to 400 km/s or above; and a narrow component, mostly seen at lower absolute RVs between 50-100 km/s (relative to  $RV_{cm}$ ), i.e. between the two bands delimited by grey lines near the center. In [S II] (red/blue curves) no wide wings are seen, but the narrow components may sometimes appear, at RVs close to those of H $\alpha$  narrow wings. A wide variety of situations is encountered across the Nebula: both the wide and narrow wings span a wide range of intensities, and each type may be observed without the other (see e.g., panels *f* and *h*). The wide wings present a marked symmetry between the blue and red sides, while the narrow wings much less so: the red wings may be stronger than the blue one, or viceversa (panels *b* and *c*). When the [S II] emission is present, although it resembles the emission in the narrow H $\alpha$  wings, it may be found at absolute RVs both lower (panel *a*) and higher (panels *d, g*) than this latter; in panel *g* it is very strong in relative terms. Finally, panel *e* shows a conspicuous case (not the only present) of self-absorption in the inner portion of the blue wide wing, at about -100 km/s; the width of this absorption component is considerable, being  $\sim 50 \text{ km/s}$ . In this section we try to understand the physical meaning of all these features.

In the Figure, one may also note a regular saw-tooth pattern in the residuals near  $RV=0$ : this is not random noise, but a systematic effect. The maximum amplitude of such residual pattern, compared to original line peaks (see Figure caption), is of order of 1-2%, in accordance with the very good appearance of fitted models in Fig. 3. From numerical experiments, it turns out that this effect arises because no wide emission component was included in our fitting model, in addition to the two gaussian com-

<sup>4</sup> The 380 km/s boundary was chosen so that the measurement of wide-wing intensity below remains unaffected by the skyglow feature falling at  $RV \sim -420 \text{ km/s}$ .

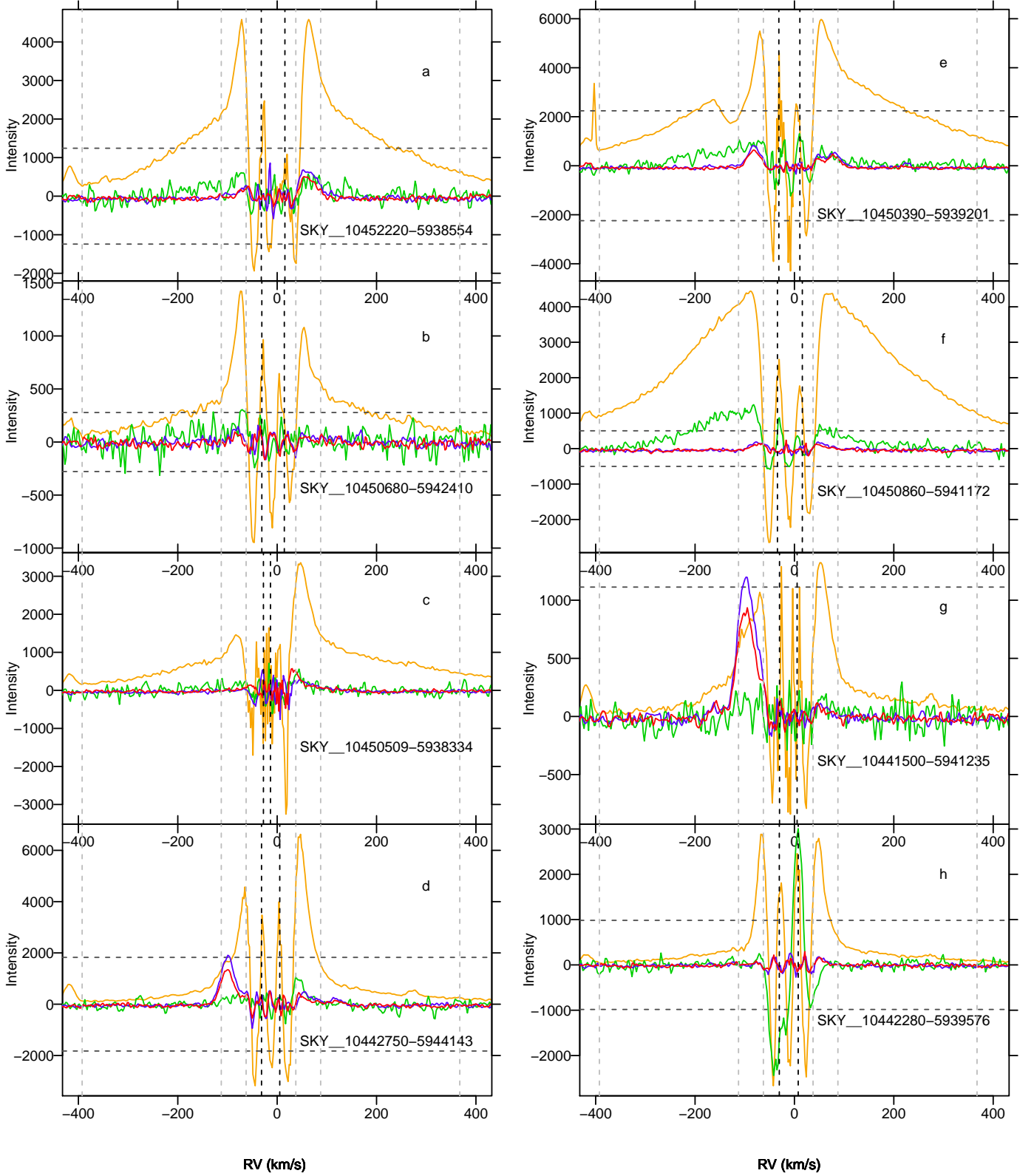


**Fig. 17.** Examples of low-intensity components in the lines, as residuals from the gaussian best fits to the main components of H $\alpha$  (orange), He I 6678 (green), [S II] 6717Å (blue) and 6731Å (red). The He I residuals are scaled up by a factor of 10, and those of [S II] by a factor of 3. Black vertical dashed lines indicate the RVs of the two main gaussian components. Grey dashed lines indicate the adopted boundaries to define the wide and narrow H $\alpha$  wings, all centered at RV = -12.5 km/s. Indicated radial velocities are heliocentric. The emission features in the H $\alpha$  profiles at RV  $\sim$  -420 and  $\sim$  +280 km/s originate from terrestrial airglow. In the plotted units, H $\alpha$  peak emission before best-fit subtraction is for each panel respectively equal to 124300 (panel a), 27800 (b), 426700 (c), 182600 (d), 224200 (e), 50200 (f), 111300 (g), and 98300 (h). Intensity levels of  $\pm 1\%$  of peak emission are indicated in each panel by horizontal dashed lines.

ponents: as a result, the widths  $\sigma$  of the best-fitting gaussians are very slightly overestimated (by  $\sim 1.5\%$ ), producing exactly the same residual pattern as observed. This affects marginally only the immediate neighborhood of the main components, and therefore also the inner boundary of the narrow  $H\alpha$  components; further out, however, the residual line profiles are totally unaffected. Incidentally, if we are able to detect systematic effects in the best-fit widths  $\sigma$  of such a small amplitude, random errors on  $\sigma$  are necessarily much smaller than 1% on average, since otherwise they would mask the above effect. In general, even where wide wings are not detected, additional components of low-amplitude, compared to the main ones, will produce similar residual patterns, especially in  $H\alpha$ . Therefore, we consider questionable the physical existence of gas emitting in the narrow  $H\alpha$  wings. Instead, the emission features in the [S II] residuals between (absolute) velocities 50-100 km/s, of amplitude much larger than the [S II] residuals in the range  $[RV_{cm} - 50, RV_{cm} + 50]$  km/s, can be considered as a real phenomenon.

We remark that Walborn et al. (2002) have found many RV components (in absorption) in the STIS UV spectra of four O stars in Carina, in lines of several ionized species: for most lines, however, the STIS spectra are saturated in RV range studied in the present paper, and provide no useful information, while the many narrow absorption components at  $RV < -100$  km/s found in the STIS spectra have a completely different appearance than the high-velocity components studied here, and therefore originate in different regions.

The existence of the wide  $H\alpha$  wings was already known for decades (Lopez and Meaburn 1984); in the direction of the Keyhole nebula, Walborn and Liller (1977) and Boumis et al. (1998) found that they are the spectrum of  $\eta$  Car, reflected from local dust. This explains the apparent self-absorption at  $RV \sim -100$  km/s, seen in Fig. 17 (panel e), and in a few other places near to that position. We will discuss in the next section the spatial distribution of the wide-wing emission, which is strongest in coincidence with the Keyhole and along the line between it with  $\eta$  Car, as found by Boumis et al. (1998). This again suggests reflected emission from  $\eta$  Car for their origin, rather than local high-velocity gas. Our data enable us to test further these two alternative hypotheses. A detailed comparison with the actual spectra of  $\eta$  Car can be done using data from the ESO archive, where 16 UVES spectra are available covering the years 2002-2004; of them we only consider those (eight) without strong signs of saturation in  $H\alpha$ . A representative selection is shown in Figure 18, in the regions around  $H\alpha$  and He I lines. We looked for similarities between our residual patterns of Fig. 17 and the  $\eta$  Car spectra in the HR15N wavelength range. The most characteristic features seen in the  $\eta$  Car spectra are the wide  $H\alpha$  wings and a peculiarly-shaped He I 6678 line, as seen in Fig. 18. Like  $H\alpha$ , also the profile of the  $\eta$  Car He I 6678 line is variable. We find a striking similarity between the latter line profiles and our He I fit residuals of Fig. 17, panels a, e, and f, and some hint of blue-wing He I residual emission also in panels b and g. This would support the case for wide  $H\alpha$  wings as a reflection effect even more. We will show below that there is no proportionality between the sky continuum intensity (from reflection nebosity) and the wide-wing intensity. This can be reconciled with wide wings being due to reflection of  $\eta$  Car emission only if the sky continuum is larger than the scattered  $\eta$  Car continuum, due to other stellar continua contributing as well. We find that this is indeed the case: Figure 19 shows that the  $\eta$  Car continuum and wide wings (downscaled by a suitable factor) describe well the lower envelope of nebular datapoints. Therefore, the missing

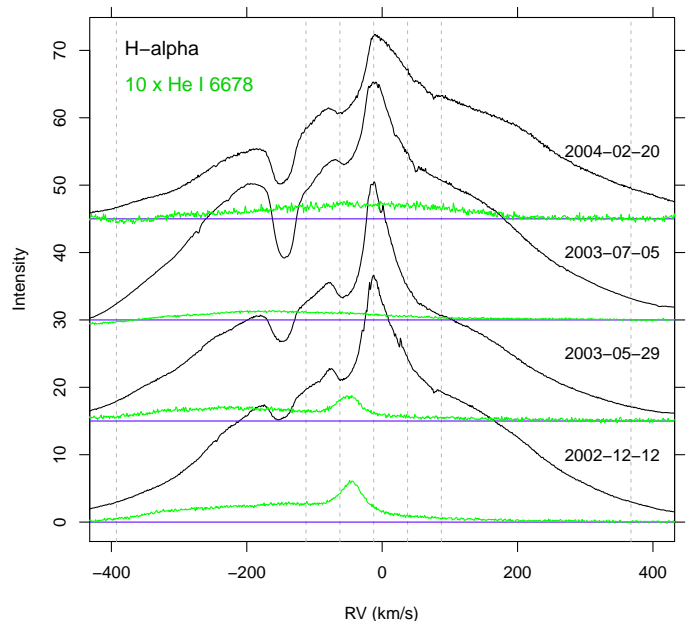


**Fig. 18.** Selection of UVES spectra of  $\eta$  Car, in the  $H\alpha$  (black) and He I 6678 lines (green), over the years 2002-2004, as indicated above each spectrum. Spectra are continuum-subtracted, and shifted vertically for clarity. The He I line amplitude was enlarged 10 times to facilitate comparison with  $H\alpha$ . Vertical dashed grey lines indicate the same velocities as in Fig. 17.

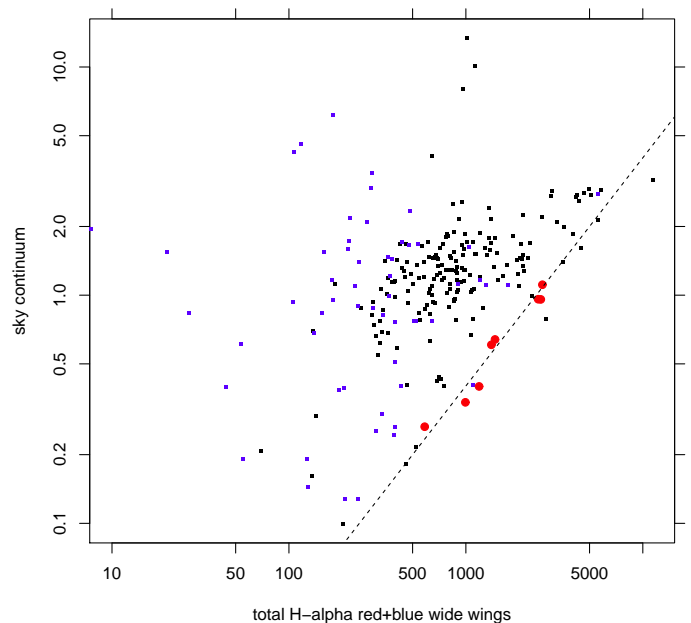
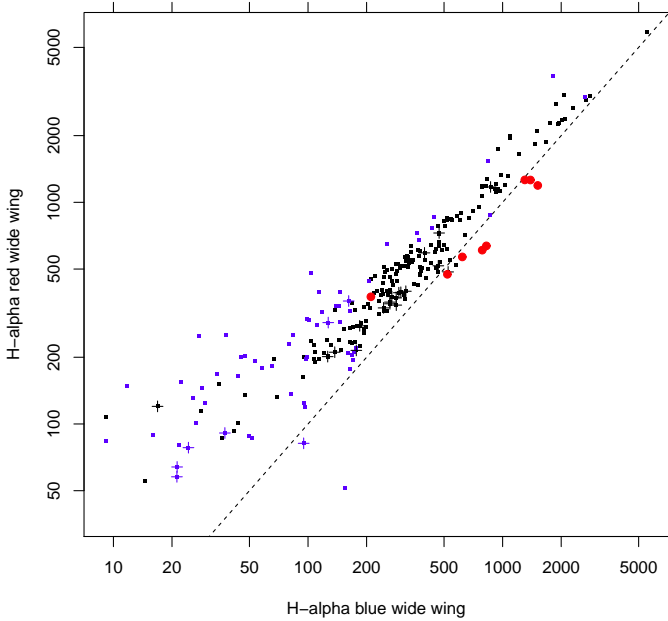


**Fig. 19.** Sky continuum vs. total intensity in the wide  $H\alpha$  wings. Small dots refer to pure-sky fibres from setups HR15N (black) and HR14A (blue), while big red dots are the (downscaled) continuum and wide wings of  $\eta$  Car. The dashed line is a constant factor of  $4 \cdot 10^{-4}$ .

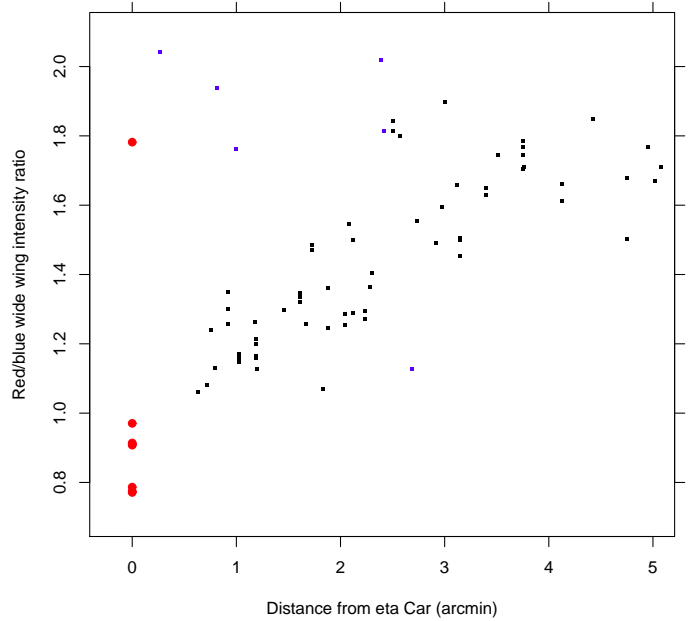
correlation between the two quantities across the nebula is not inconsistent with the reflection hypothesis for the wide wings.

Figure 20 shows that, as already suggested from Figure 17, the intensities in the blue and red parts of the wide  $H\alpha$  wings are very well correlated with one another. Figure 20 also shows that the intensity in the blue wide wing is systematically lower than





**Fig. 20.** Intensity of red vs. blue wide  $H\alpha$  wings. Datapoints from pure-sky fibres of HR15N (black) and HR14A (blue) setups. The dashed line is identity. The big red dots indicate the wide wings in the  $\eta$  Car spectra.



**Fig. 21.** Ratio of red to blue wide  $H\alpha$  wing intensities, in the vicinity of  $\eta$  Car, vs. radial distance. Symbols as in Fig. 20.

that in the corresponding red wing. This is actually inconsistent with most of the measurements from  $\eta$  Car spectra (red data-points); the signal-to-noise ratios of the latter spectra is so high that the errors on the  $\eta$  Car wing measurements are negligible (comparable to the plotted symbol size), so that the difference is highly significant. Also significantly different are the velocities of the absorption reversal in the  $\eta$  Car spectra ( $v \sim -150$  km/s) and in the nebular spectrum ( $v \sim -125$  km/s) of Fig. 17, panel *e*. Both discrepancies can be reconciled, however, by assuming that the scattering dust is not at rest. If the dust is expanding away from  $\eta$  Car it will “see” its  $H\alpha$  emission as redshifted; then, depending on the dust relative motion with respect to us, the reflected redshifted line may gain an additional redshift, a blueshift, or no shift at all. For a spherically expanding dust envelope, a total wavelength shift varying linearly with radial distance is predicted. Therefore, Figure 21 shows the ratio between the red and blue wide  $H\alpha$  wings (increasing with redshift), vs. radial distance from  $\eta$  Car: a clear correlation is seen for most datapoints, connected smoothly with the actual  $\eta$  Car values at zero distance. No such correlation is instead found for distances  $> 5$  arcmin from  $\eta$  Car. It should be remarked that because of the variability found in the  $\eta$  Car  $H\alpha$  profiles (red points), some scatter in the distribution of nebular values was expected, in agreement with the handful of outliers seen in the Figure. Therefore, the hypothesis of a reflection origin for the wide  $H\alpha$  wings is supported by our data only if the scattering dust is radially expanding away from  $\eta$  Car. On the other hand, we do not find any reasons why the emission from genuine high-velocity gas should show a pattern like that in Fig. 21: therefore this latter hypothesis should be discarded. It should be also remarked that the reflecting dust is likely to form a half shell expanding towards us, rather than away from us: in the latter case, dust observed close to  $\eta$  Car would move away both from this star and from us, and the corresponding redshift in the scattered emission would be larger than the redshift at the shell edge further away, where dust moves tangentially with respect to us. Therefore, a

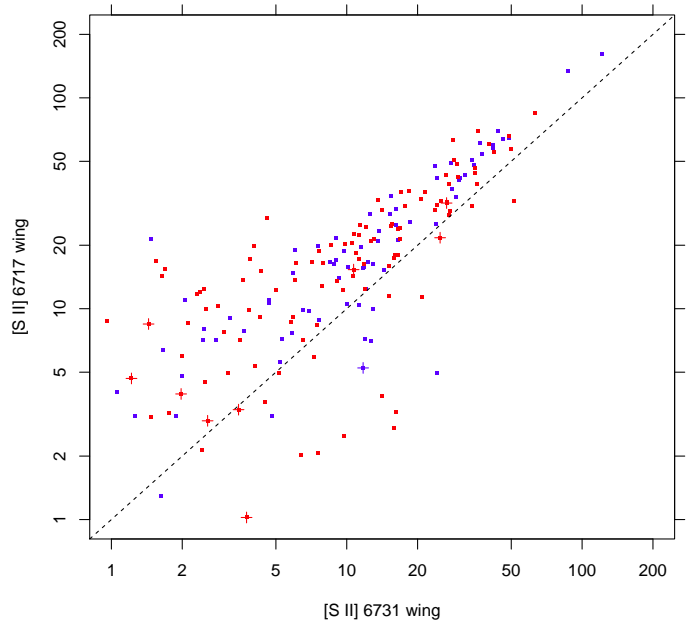


**Fig. 22.** Intensity of high-velocity components in the [S II] 6717 Å line vs. those in the [S II] 6731 Å line. The dashed line is identity. The average ratio, larger than one, indicates low densities. Symbols as in Fig. 10.

dust half-shell expanding away from us should show a negative slope in the redshift-radius diagram, whereas the positive slope seen in the diagram of Fig. 21 corresponds to a half-shell expanding towards us.

All considered, the most reliable indicator of genuine diffuse high-velocity gas ( $v \sim \pm 100$  km/s), found only at some places in the studied region, is the occasional emission in the [S II] wings discussed above. The doublet ratio permits to derive the gas density of this high-velocity gas. Figure 22 shows the intensity in

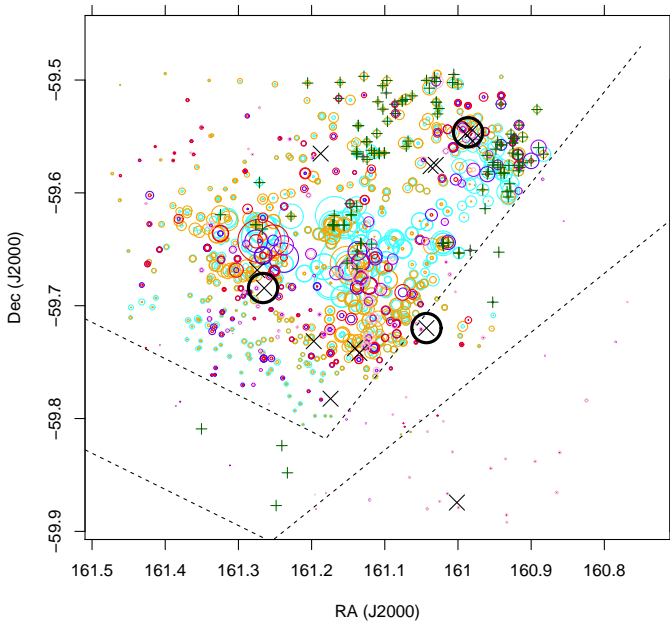


**Fig. 23.** Spatial map of  $H\alpha$  line intensity (fit normalization). The radius of each circle is proportional to intensity. Blue (cyan, purple) circles refer to the approaching component, while red (orange, pink) circles refer to the receding component. Circle color codes as in Fig. 7 and 12. The oblique dashed lines outline the edges of the absorption lanes visible in Fig. 1. Crosses indicate the positions of O/WR stars from Walborn (1973). Thick black circles indicate the positions of Trumpler 14 (upper),  $\eta$  Car (middle left), and the Wolf-Rayet star WR25 (middle right). The green '+' symbols indicate positions of "zero-velocity" gas, defined from Fig. 4.

[S II] 6717Å vs. [S II] 6731Å: the former is on average larger, indicating low densities ( $\sim 100 \text{ cm}^{-3}$ ).

### 3.3. Spatial morphology

Important information on the emitting gas is derived from its spatial distribution. Figure 23 shows a map of the intensity of the two main components (blue/cyan/purple circles for the approaching component, red/orange/pink circles for the receding one). The circle radius is proportional to the best-fit normalization (scaled by exposure time, and thus proportional to observed flux). The dark lane position is indicated by the dashed lines. Crosses indicate O/WR stars from Walborn (1973). Thick black circles indicate the positions of Trumpler 14 center,  $\eta$  Car, and the Wolf-Rayet star WR25. Finally, green plus symbols indicate positions of "zero-velocity" gas identified in Figure 4.

Figure 23 is very complex, but a few dominant features can be observed. The distribution of surface brightness is not the same for the approaching and receding components: this latter strongly dominates especially in a region comprising  $\eta$  Car and towards Southwest, parallel to the southern dark lane. The approaching component dominates North of this region, and also between it and the southern dark lane, with impressive systematicity despite the low intensity of both approaching and receding components there. Most of the zero-velocity gas is found concentrated on two sides of Trumpler 14, again parallel to the nearest dark lane. Overall, it is evident that plane-parallel distributions prevail here over circular (spherical) configurations for the bright material, as it was already clear for the dark, obscuring material. Some sort of density stratification probably plays a

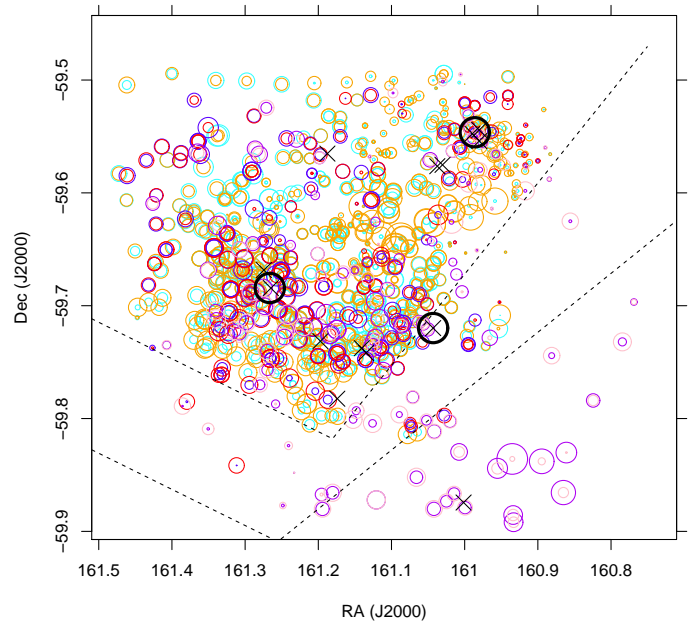


**Fig. 24.** Map of RV of approaching and receding gas. Symbols as in Fig. 23. Circle size is proportional to  $|RV - RV_{cm}|$ , with the largest circle corresponding to  $|RV - RV_{cm}| = 42.6 \text{ km/s}$ .

very important role in shaping the entire central region of the Carina Nebula. We remark that the different intensity distributions for the two components could have never been discovered using narrow-band  $H\alpha$  images, since even narrow-band filters are not wavelength-selective enough to image them one at a time.

Figure 24 is a map similar to Fig. 23, but with circle radii proportional to  $|RV - RV_{cm}|$  for both approaching and receding components. As already suggested from the discussion on Fig. 4 there is no global velocity pattern; on smaller scales, we observe again the near zero RVs on the two sides of Trumpler 14, and there are indications that other patterns exist on similarly sized scales. Therefore, the two main components here must be local to the inner region of the Nebula, and not connected to the global expansion of the whole Carina nebula, on scales of 20-30 pc, as already discussed above.

Before discussing the local regions individually, we examine some more distribution maps. Figure 25 illustrates the distribution of wide  $H\alpha$  wings intensity (grey circles, with radii proportional to intensity): it is clear that they are found all around  $\eta$  Car, not only in the direction of the Keyhole Nebula. The green circles instead indicate the intensity of the sky continuum, which is distinctly measurable in some of the pure-sky spectra, and reveals reflection nebulosity from dust in the vicinity of bright stars. The fact that this continuum emission has no features similar to the solar spectrum, and that its intensity varies among sky spectra from the same OB, ensures that it is not originating from scattered moonlight, but from dust reflection in Carina. The strongest reflection nebulosity is evidently found in Trumpler 14, but also the  $\eta$  Car region shows clear detections of it. As discussed in the previous section, we do not find a proportionality between the intensity of the reflected sky continuum and that of the wide  $H\alpha$  wings.

Then, Figure 26 shows the spatial distribution of the intensity ratio between the [N II] 6584Å line and  $H\alpha$ . However, since we found above that the respective dynamics of hydrogen and nitrogen show that the two sets of lines do not come from exactly the

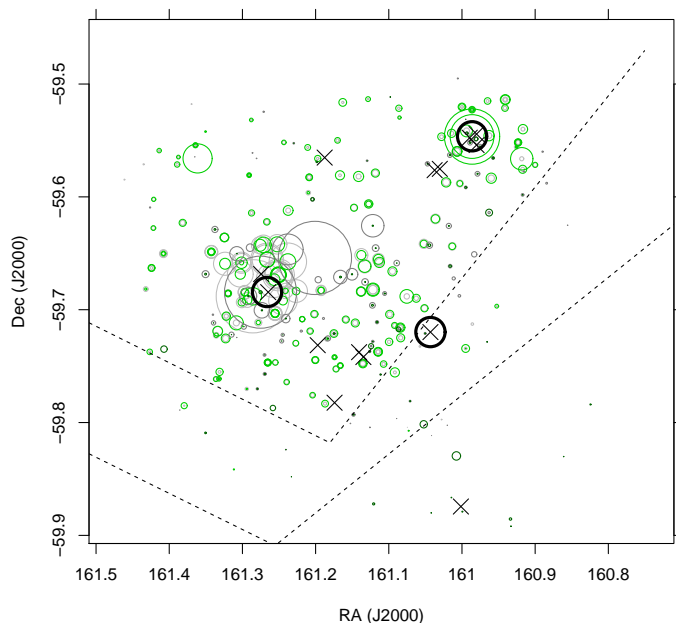


**Fig. 25.** Map of the distribution of intensity in the wide  $H\alpha$  wings (grey) and sky continuum emission (green). Circle size is proportional to intensity. Darker grey circles indicate data from pure-sky fibres using HR14A setup. Thick circles and crosses have the same meaning as in Fig. 23. The large grey circle closest to center indicates the very intense  $H\alpha$  wings in the direction of the Keyhole nebula.

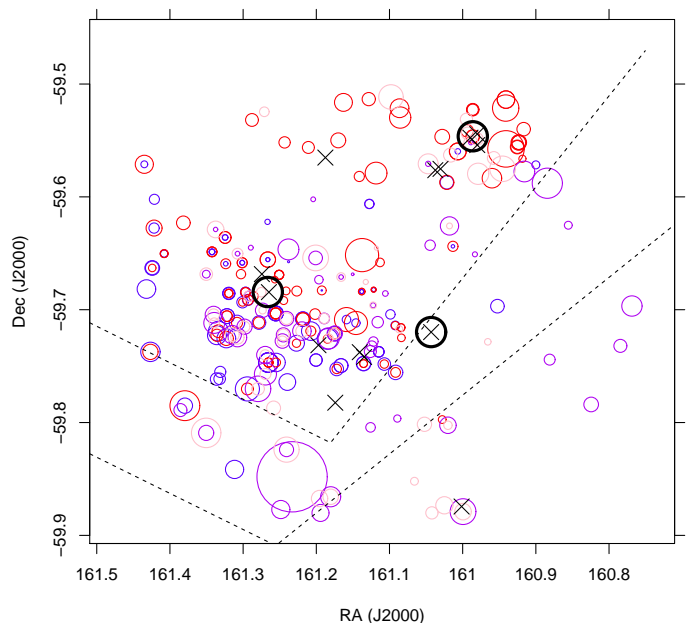


**Fig. 26.** Map of the intensity ratio  $[N II] 6584\text{\AA}/H\alpha$ . Symbols as in Fig. 23, except for the (cyan/orange) data from faint stars, not used here. Circle size is proportional to ratio, with largest circle corresponding to a value of 2.4.

same gas but merely from adjacent (or otherwise loosely connected) gaseous components, we consider their intensity ratio only in places where their RVs differ by less than 3 km/s. For constant ionization fractions of H and N, their intensity ratio is an increasing function of gas temperature (Haffner et al. 2009). Taking it at face value, under the hypothesis of constant H and N ionization, the map would imply a wide range of temperatures for the emitting regions (about a factor of 3, with exact values depending on the assumed H and N ionization fractions). This is wider than the range derived above from the line-width ratios (outliers excluded), and moreover there is no correlation between the line-width ratios and the N/H intensity ratios shown in Figure 26. Therefore, it is more likely that rather than a range in gas temperatures the ratios N/H reflect here variations in the N (or H) ionization fraction. The Figure shows then that this varies strongly, and in different ways for the approaching and receding components (as found by Deharveng and Maucherat 1975): in the approaching component the N ionization increases markedly south of  $\eta$  Car (again, along a region parallel to the southern dark lane), while in the receding component it is more uniform, with some preference for higher values in the northern parts. We will discuss an interpretation of this fact in the next section.

Figure 27 shows the distribution of the intensity ratio between  $[S II] 6731/6717\text{\AA}$  (increasing with density), of which the largest values are especially found in the region surrounding the Keyhole nebula. Finally, Figure 28 shows the intensity distribution of the high-velocity  $[S II]$  emission occasionally found (see Fig. 17), which is especially frequent as a receding component North of  $\eta$  Car, and as an approaching component next to the Western lane, and may trace high-speed shocks (Hartigan et al. 1999). A closer examination of shock diagnostics will be presented in Section 3.5 below.

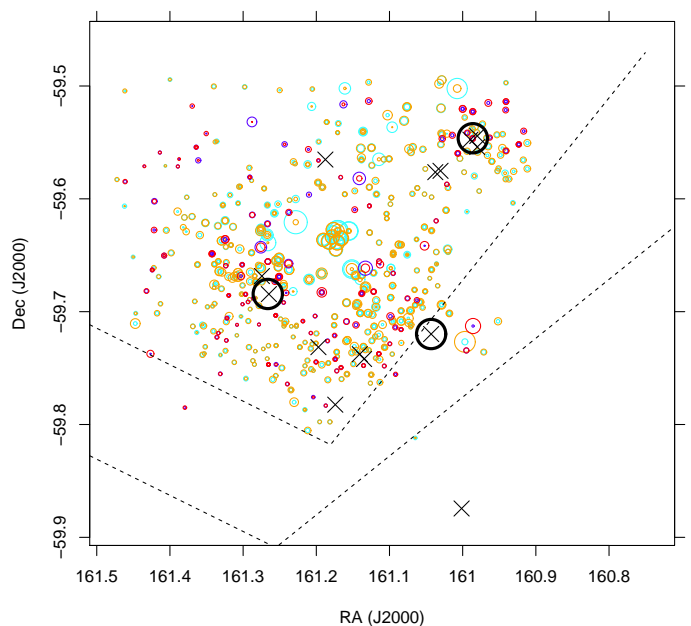


**Fig. 27.** Map of the intensity ratio between  $[S II] 6731/6717\text{\AA}$ , increasing with density. Symbols as in Fig. 23. Largest circle corresponds to a ratio of 0.65. Note the large values of this ratio near the Keyhole nebula,  $\sim 3$  arcmin N-W of  $\eta$  Car.

### 3.4. Position-velocity diagrams of shell-like structures

As discussed above with reference to Figs. 23 and 24, velocity structures seem to exist at local scales, rather than on the scale of the entire studied region. It was also remarked that plane-parallel geometries are dominant over circular ones, so it becomes natural to look for velocity structures along preferred directions, rather than along the radial direction inside circular re-

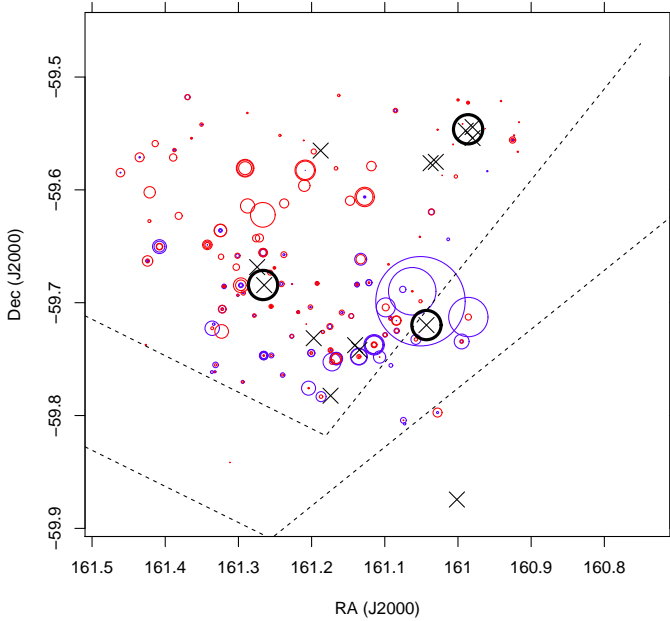


**Fig. 28.** Map of intensities of emission in the far wings of [S II] 6717. Symbols as in Fig. 23.

gions. The first example shown here in Figure 29 is a position-velocity diagram in the region surrounding the Northern cluster Trumpler 14, already mentioned in connection to the zero-velocity gas. In Fig. 29, the abscissa reports position along an axis at position angle of  $110^\circ$  (from North, clockwise), passing through Tr 14 center. The chosen position angle reflects the spatial alignment of zero-velocity datapoints. The circle radius is proportional to  $H\alpha$  intensity (fit normalization), and approaching and receding components are both indicated with the same colors. The pattern indicates some sort of radial expansion, approximately centered in Tr 14. The geometry is not spherical, however, but distorted, probably because the medium into which expansion is taking place has strongly non-uniform density. Some non-spherical expansion geometry was already suggested by Deharveng and Maucherat (1975). We find an abrupt discontinuity in the RV pattern for the approaching component at projected distances between  $(-2, -1)$  arcmin: to the left of this position, the approaching gas RVs flatten out to a nearly constant value close to  $-10$  km/s, as if the expanding gas had hit a much denser layer of material traveling at that speed, and was basically stopped and forced to co-move with it.

Additional evidence for such an interaction having occurred between the expanding gas and another layer may come from the position-velocity diagram of Figure 30, which differs from the previous Figure in that the circle size is proportional to  $H\alpha$  line width  $\sigma$ , and thus to turbulent speed (or temperature): it is clear from this latter diagram that the line width increase systematically and significantly in the “stopped” gas, likely as a result of a collision with a massive obstacle. Also interesting is the corresponding position-velocity diagram using [N II] instead of  $H\alpha$ : in fact, in this region are found many of the outliers seen in Fig. 10, where the  $H\alpha$  RV was near  $RV_{cm}$  while the RV of [N II] emission was similar to the rest of the approaching gas. Analogously, Figure 31 shows that the expansion of the Tr 14 shell seen in the [N II] line is very different than seen in  $H\alpha$ : the shell morphology is barely discernable, and more importantly the [N II] emission does not indicate any slowed-down expan-

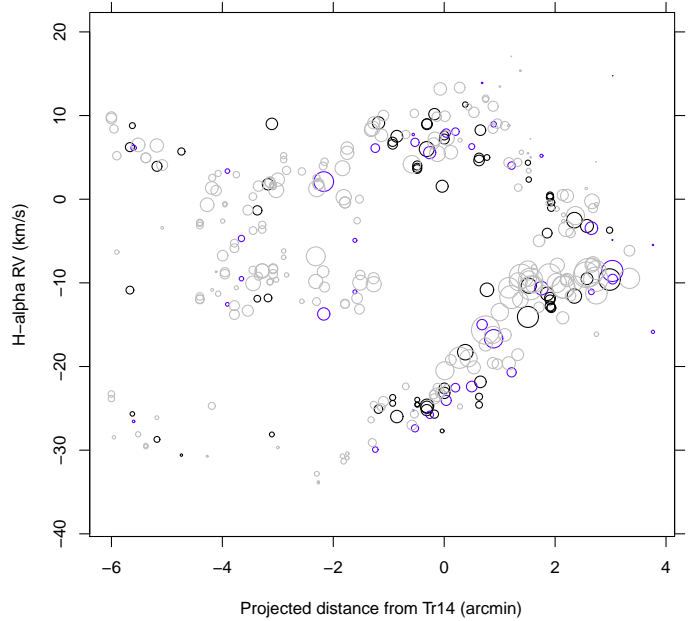


**Fig. 29.** Position-velocity diagram for  $H\alpha$  in the neighborhood of Trumpler 14. Circle size is proportional to line intensity. Color codes as in Fig. 4. The distance origin is taken at the Trumpler 14 position indicated with the big black circle in the upper right of Fig. 23. Positive distances are towards S-W; the dark lane lies at position  $\sim +3$  arcmin. Direction of the observer is towards the bottom, at negative RVs.

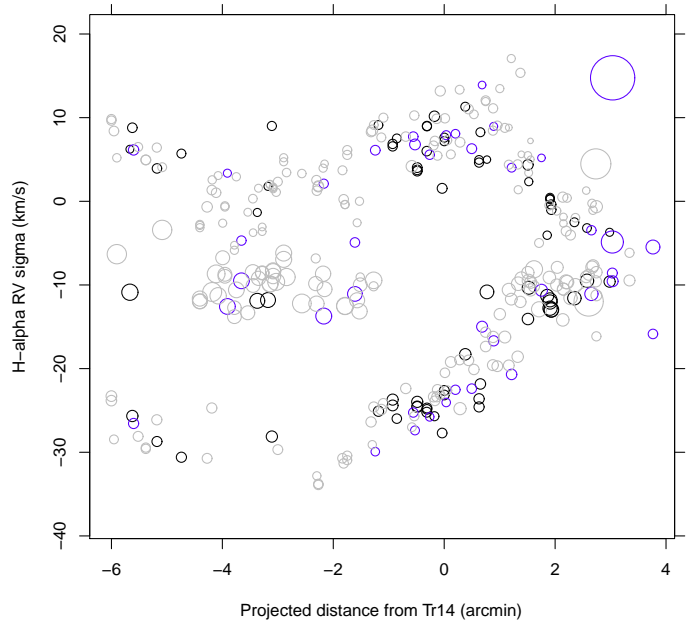


**Fig. 30.** Same as Fig. 29, except that circle size is here proportional to line width  $\sigma$ .

sion where  $H\alpha$  does, but continues to show large approaching velocities. Obviously, the [N II] emitting gas is different, and in this particular case lying beneath the gas emitting  $H\alpha$ , and has yet to reach the space region where slowing-down occurs.

Also worth investigating is the region surrounding  $\eta$  Car, as remarked in the discussions above on spatial distributions. Figure 32 is a velocity-position diagram like Fig. 29 but centered on  $\eta$  Car, towards position angle  $35^\circ$ . Here too a sort of dis-



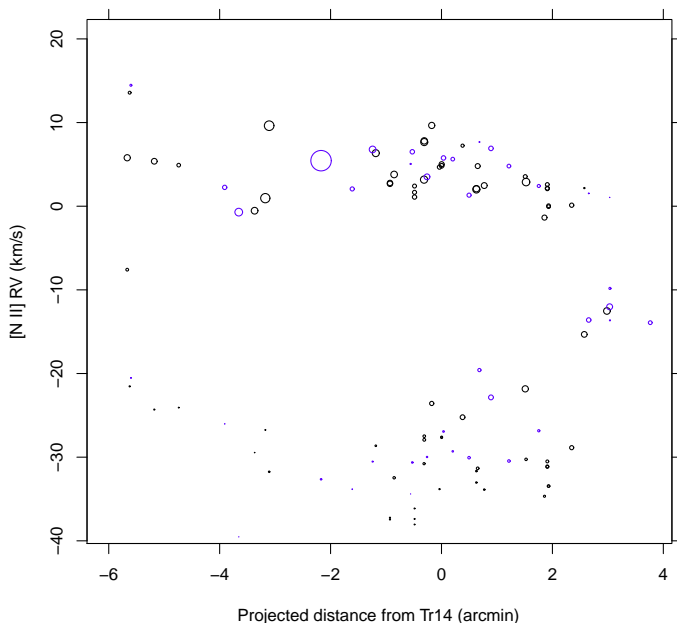


**Fig. 31.** Same as Fig. 29, but using the [N II] 6584 Å line.

torted, incomplete shell is suggested by the diagram: the incompleteness towards South is due to the strong obscuration by the southern dust lane (left of distance of -5 arcmin in the Figure). At projected distance  $\sim 2.5$  arcmin the shell border, converging towards  $RV_{cm}$ , is clearly visible; the same datapoints show increased  $H\alpha$  line intensities (larger circles in the Figure), as expected because of projection effects. This position nearly coincides with the Keyhole nebula. To the right of this position,  $H\alpha$  emission is much weaker, but the RV pattern suggests the existence of another shell towards NNW, possibly centered on the O3 star HD93250. Near position  $\sim 2.5$  arcmin, an interaction between the two shells might be taking place, and contributing to the peculiarities of the Keyhole nebula summarized in Smith and Brooks (2008). Such an interaction might be diagnosed by an increased gas turbulence, which as can be understood from Fig. 9 is an important contributor to measured line widths. To investigate this possibility we show in Figure 33 the same diagram with circle sizes proportional to  $H\alpha$  line widths: these are generally small (symbols adopt the same scaling factor here as in Fig. 30), but increase precisely in the group of datapoints around position  $\sim 2.5$  arcmin and  $RV \sim -10$  km/s, i.e. the putative interaction region between the shells. This might be an indication of ongoing shell collision and merging.

The  $\eta$  Car shell presents a rich phenomenology which deserves a closer examination. As evident from Fig. 26, in the half-plane S-E of  $\eta$  Car the [N II]/ $H\alpha$  intensity ratio is systematically larger in the blueshifted component than in the redshifted one. Moreover, under the rough zero-order assumption of spherical expansion, we can transform the line RV into a distance from the expansion center (i.e.,  $\eta$  Car), with a best-guess conversion factor such that the shell is as round as possible in shape. The result of this transformation is shown in Figure 34, where axes are scaled to parsecs using the known Nebula distance; the original measurements (sky-projected distance in arcmin and RV) are shown at top and right borders, respectively. Only components which differ in RV by less than 3 km/s are used to compute the [N II]/ $H\alpha$  ratio (proportional to symbol size in Fig. 34). We know the inclination angle to the line of sight of the Homunculus Neb-

ula surrounding  $\eta$  Car (whose two lobes are indicated in Fig. 34 in brown color) from the very detailed studies of Davidson et al. (2001) and Smith (2006). It turns out that the  $H\alpha$ /[N II] ratio varies in a systematic way with azimuthal angle  $\theta$ , defined in the Figure (and increasing counterclockwise), with  $\theta = 49^\circ$  corresponding to the projection of the Homunculus polar axis in the N-W direction (with a component away from us), and  $\theta = 229^\circ$  corresponding to its projection towards S-E (with a component towards us). As a function of  $\theta$ , the  $H\alpha$ /[N II] ratio is shown in Figure 35: fairly well-defined minima are found corresponding to each of the poles. In the next section we will discuss that the  $H\alpha$ /[N II] intensity ratio may be considered a good indicator for the ionization parameter  $q$ . Thus, the minima in Fig. 35 also correspond to minima in the ionization parameter  $q$ : gas lying along the Homunculus polar axes is therefore irradiated with much less UV flux than gas in the equatorial directions ( $\sim 30$  times less). This is possible if the total column density in the matter surrounding  $\eta$  Car is not isotropic, but much higher near the polar axes. This picture agrees very well with the findings of Smith (2006), that most of the matter forming the Homunculus was originally ejected by  $\eta$  Car at high latitudes, and did not get its shape by the effect of a circumstellar torus. If this latter picture was the case, we would have observed a brighter UV irradiation near the poles, i.e. the opposite of what our data suggest. Our picture also implies that  $\eta$  Car is by far the dominant ionizing source inside its own shell, and probably throughout the entire Trumpler 16 cluster.

Such directionality in the ionization pattern around  $\eta$  Car, and the shape itself of the Homunculus, would suggest a polar-angle dependence also for the mechanical energy output of  $\eta$  Car winds. If this is true, the fact mentioned above that the (turbulent) line widths increase near the inter-shell boundary, but not along the  $\eta$  Car polar axis, might then suggest that winds from massive stars are a secondary contributor to turbulence in  $H_{II}$  regions, in agreement with Krumholz and Burkhardt (2015).

We have also examined if a similar pattern exists for the gas density, as measured from the [S II] 6731/6717 line ratio. The corresponding diagram is shown in Figure 36, with circle sizes proportional to the [S II] 6731/6717 intensity ratio (increasing with density). Here, no dependence on closeness to Homunculus polar axis is found; instead, the line ratio and gas density tends to increase systematically from S-E towards N-W (left to right in the Figure) for projected distances  $< 3 - 4$  arcmin, with the highest densities found near the N-W shell edge, corresponding to the Keyhole nebula, as remarked above.

Finally, Figure 37 suggests the existence of a third prominent shell, centered on the Wolf-Rayet star WR25 ("WR25 shell"), with position angle  $150^\circ$ . Here too, the southern part of the shell is hidden behind the (western) dark dust lane, while at position  $\sim -2.5$  arcmin the shell boundary is seen in the diagram, with enhanced  $H\alpha$  luminosity as above. Also in this case, to the left of that boundary traces of another shell can be seen (presumably the same shell North of  $\eta$  Car as mentioned above). Here again we test using line widths if interactions may be present: Figure 38 suggests that this may indeed be the case, with increased line widths at several places near  $RV_{cm}$ . Also the much increased intensity of the [S II] lines at some places in this region, shown in Figure 39, might be indicative of localized shocks at the interface between the two shells (Hartigan et al. 1999).

All shells show a distorted shape, indicative of density gradients of the material into which they expand. For this reason it is difficult to define a typical "radius" for each of them. The maximum RV interval  $\Delta RV$  at shell center is instead clearly defined from the position-velocity diagrams, and found to be  $\Delta RV \sim 35$



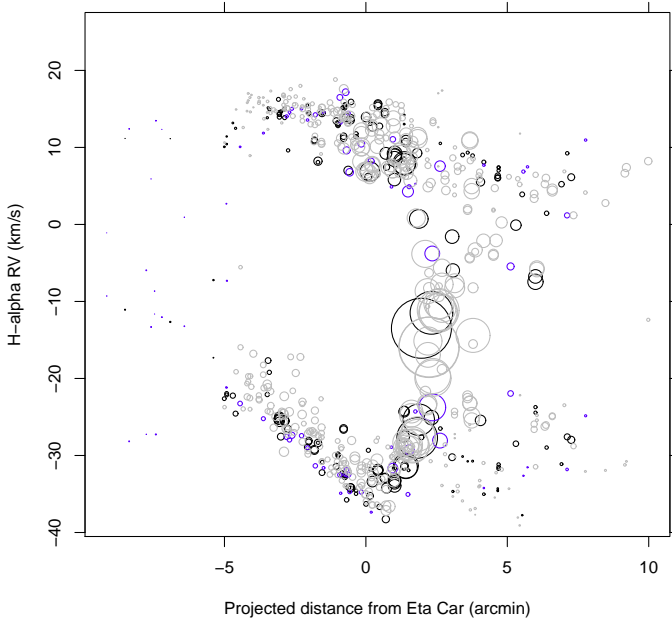


**Fig. 32.** Same as Fig.29, but centered on  $\eta$  Car. Positive distances are towards N-W direction from  $\eta$  Car. The Keyhole nebula lies at position  $\sim +3$  arcmin.

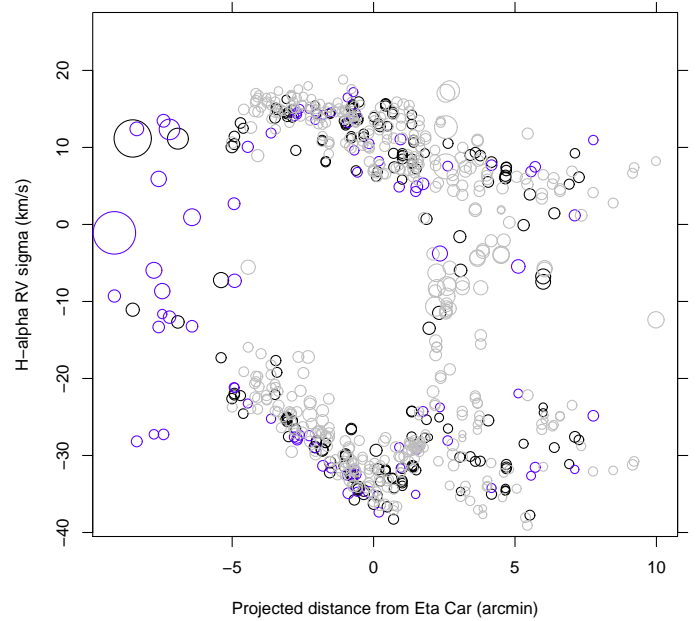


**Fig. 33.** Same as Fig.32, except that circle size is here proportional to line width  $\sigma$ .

km/s for the Tr 14 and WR25 shells, and a larger  $\Delta RV \sim 45$  km/s for the  $\eta$  Car shell. The approximate sizes of the shells ( $\sim 5$  arcmin radius) and the observed expansion speed allow to estimate a timescale, which turns out to be very short,  $\sim 1.5 \cdot 10^5$  years for the  $\eta$  Car shell. Since this is much shorter than the estimated ages of the massive stars in Carina, it is likely that a much larger amount of material should be present exterior to the bright nebula. Detection of a complex velocity structure in the interstellar absorption Na I D lines was indeed already known towards the center of Carina (Walborn et al. 2007 and references therein), and demonstrates the existence of substantial amounts of neutral gas in addition to the predominantly ionized gas studied here. The Gaia-ESO data on the Na I interstellar lines in Carina will be studied in a future work.

### 3.5. Line-ratio diagrams

In this section we discuss briefly how line ratios in our dataset compare with measurements from other nebular regions, including H II regions, Planetary Nebulae (PNe), and Supernova Remnants (SNR). Line-ratio diagrams involving the lines used in this work were presented by Sabbadin et al. (1976), and then by Riesgo and López (2006) and Viironen et al. (2007). They showed that these different object classes populate different regions in the diagrams, with minimal mutual overlap. We show in Figure 40 the intensity ratios of  $H\alpha/[N II]$  vs.  $H\alpha/[S II]$ . As is clear from Figs. 10 and 12, however, some sightlines have discrepant RVs between  $H\alpha$  and  $[N II]$  ( $[S II]$ ): whenever the RV discrepancy was more than 3 km/s in absolute value the line-ratio diagram, mixing intensities of emissions from slightly different nebular layers, must be treated with caution: corresponding datapoints are therefore shown with tiny dots. The black lines and polygons shown in Fig. 40 indicate typical loci of H II regions, PNe and SNR. None of our datapoints falls in the SNR region, where heating is dominated by shocks. The bulk of datapoints lies just above the PNe wide strip (note however that the limits of

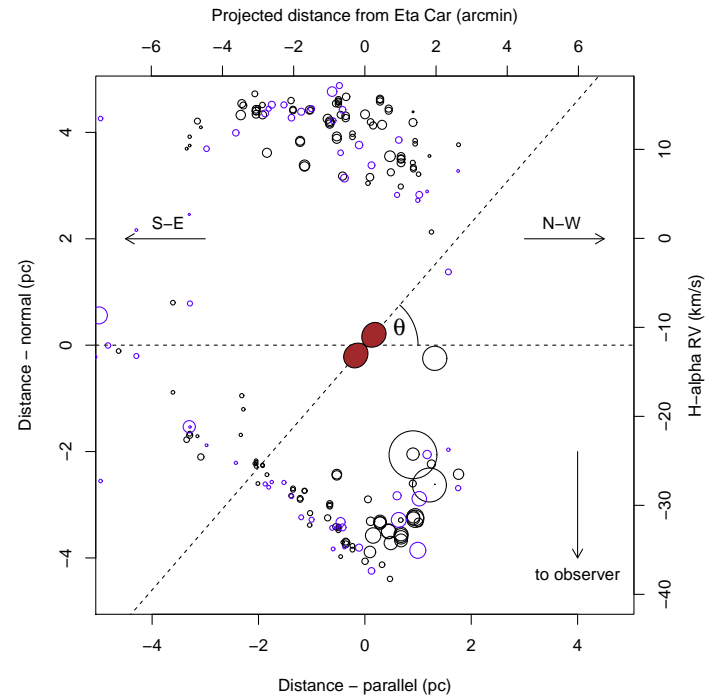


**Fig. 34.** Reconstructed geometry of the  $\eta$  Car shell. Bottom (left) axis indicates distances parallel (normal) to the plane of sky. Top and right axes indicate the original measurements, as in Fig. 32. Symbols as in this latter Figure, except that here circle size is proportional to the  $H\alpha/[N II]$  intensity ratio. The brown double-lobe structure near the center represents the position and actual inclination of the Homunculus nebula (size is not to scale). The horizontal dashed line, which defines angle  $\theta = 0$ , is parallel to sky plane, the oblique line indicates the Homunculus polar axis.

these loci are only indicative: see the much wider distributions of PNe points in Riesgo and López 2006). Nearly half of our datapoints fall outside the “nominal” H II box in the Figure: this same pattern was already found for extragalactic H II regions by Viironen et al. (2007). These latter authors compare their datapoints

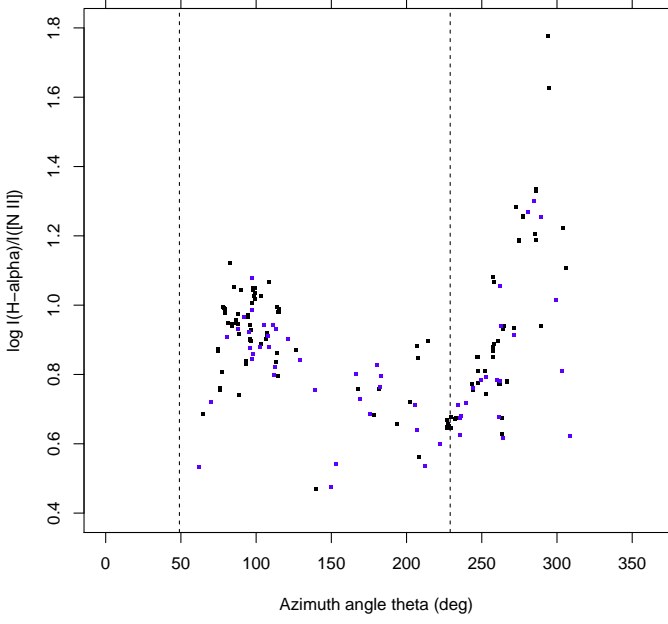


**Fig. 35.** Intensity ratio  $H\alpha/[N II]$  vs. azimuthal angle  $\theta$ , defined in Fig. 34. Symbols as in Fig. 5. Vertical dashed lines indicate the projections of the Homunculus polar axis.

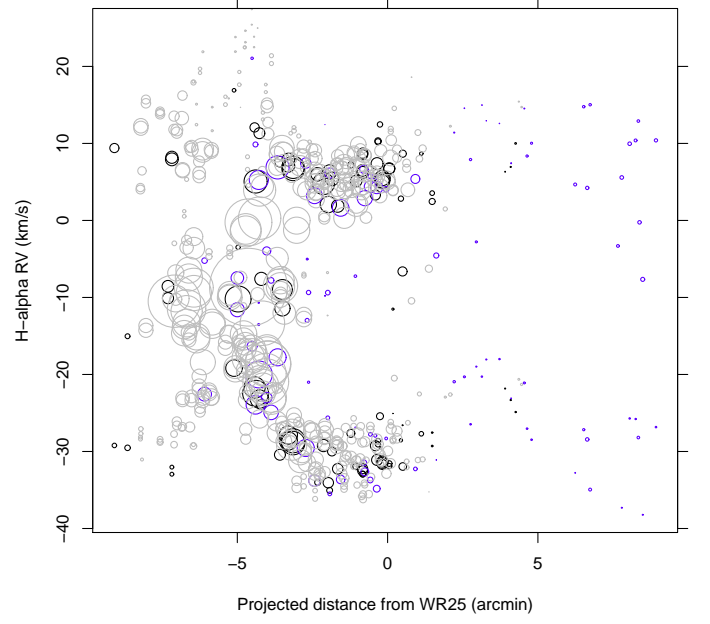


**Fig. 37.** Same as Fig.29, but centered on WR25.

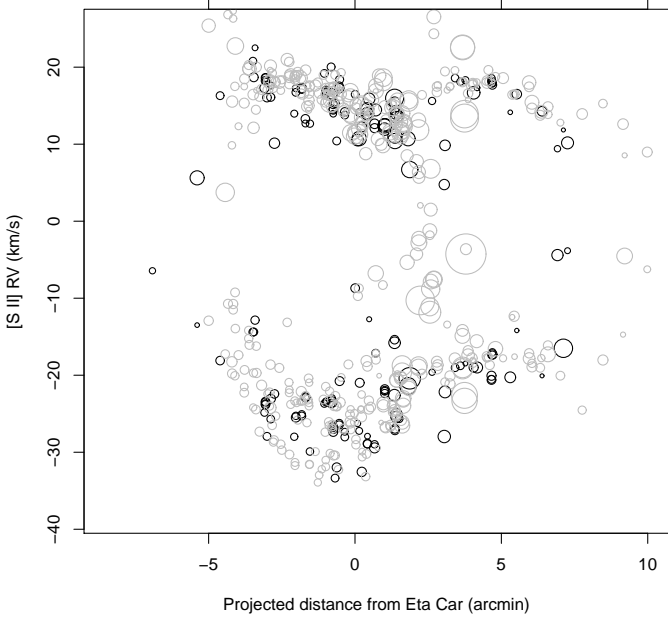


**Fig. 36.** Same as Fig.32, except that circle size is proportional to  $[S II]$  6731/6717 intensity ratio.

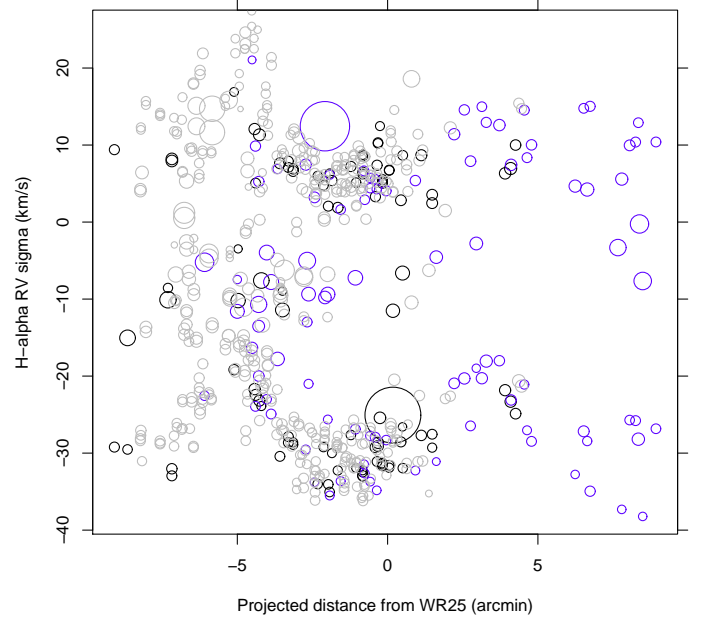


**Fig. 38.** Same as Fig.37, except that circle size is here proportional to line width  $\sigma$ .

with grids of nebular ionization models, and show that such a pattern is indeed expected for a fixed  $[O/H]$  abundance ratio, but varying ionization parameter. In particular, our datapoints agree with oxygen abundance of  $8.7 < 12 + \log(O/H) < 8.9$ , and ionization parameter in the range  $6 \cdot 10^7 < q < 10^9$ . Both  $H\alpha/[N II]$  and  $H\alpha/[S II]$  increase with  $q$  in the given range. The fact that most of our datapoints fall at higher  $H\alpha/[S II]$  values than typical Galactic  $H_{II}$  region is likely caused by the ionization parameter  $q$  in Carina exceeding typical  $H_{II}$  values elsewhere in the Galaxy.

Another useful diagram introduced by Sabbadin et al. (1976) is the  $[S II] \lambda\lambda 6717/6731$  intensity ratio vs.  $H\alpha/[S II]$  (Figure 41). Here again loci of  $H_{II}$  regions, PNe and SNR are indicated. This diagram contains more datapoints than that of Fig. 40 since it is based on three lines only, not involving  $[N II]$ . In addition, we include measurements (circles) from narrow line wings (section 3.2), which are sometimes very evident in  $[S II]$ . Plus signs indicate instead zero-velocity gas, which may lie at the interface between adjacent shells. Fig. 41 shows that a handful of datapoints from these two latter categories lie in the SNR region or very close to it, suggesting that shocks may indeed be

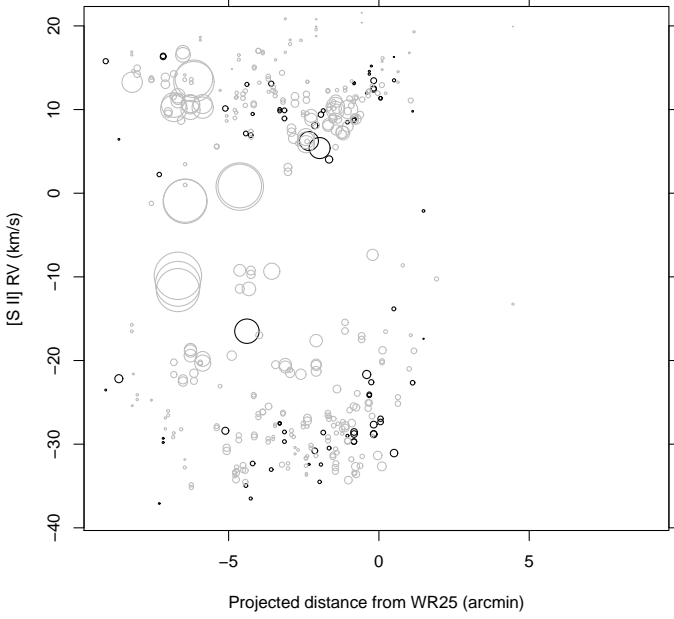


**Fig. 39.** Same as Fig.37, but now using [S II] 6731Å intensity.

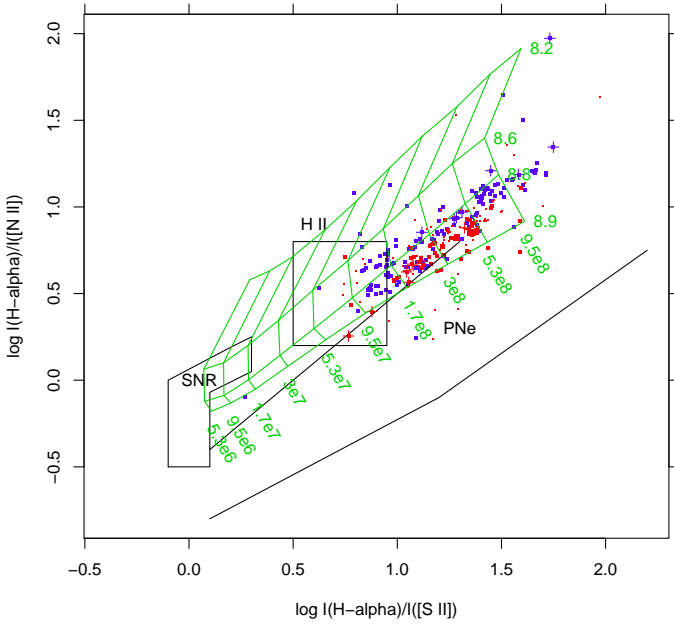


**Fig. 40.** Plot of intensity ratios  $H\alpha/[N II]$  vs.  $H\alpha/[S II]$ . Symbols as in Fig. 7. Tiny dots indicate measurements where the absolute RV difference between  $H\alpha$  and  $[N II]$ , or  $H\alpha$  and  $[S II]$ , is larger than 3 km/s. Black lines/polygons indicate typical loci of Supernova Remnants (SNR), Planetary Nebulae (PNe), and Galactic  $H II$  regions (H II), as labeled. The green line grid is part of the CLOUDY model grid shown in Viironen et al. (2007), over a range of O/H abundances and ionization parameters  $q$ , as labeled.

present, but only in very few places in the nebula, including the shell boundaries.

#### 4. Discussion

The new observations of nebular emission lines in the central regions of the Carina Nebula have put into evidence a rich va-

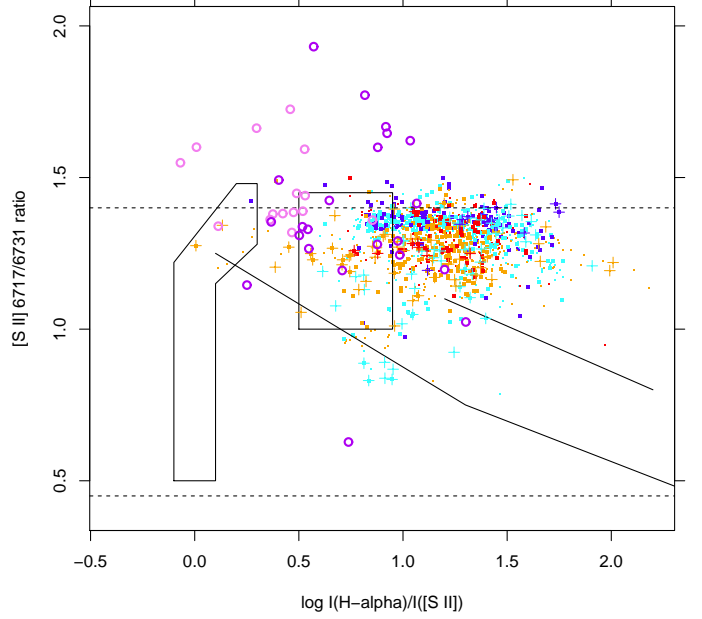


**Fig. 41.** [S II]  $\lambda\lambda$  6717/6731 intensity ratio vs.  $H\alpha/[S II]$  ratio. Circles refer to intensity ratios in the narrow wings of [S II] and  $H\alpha$ , when present (violet: approaching; purple: receding component). Other symbols as in Fig. 12. Solid lines/polygons indicate SNR,  $H II$  and PNe loci as in Fig. 40. Dashed horizontal lines enclose the range where the [S II] 6717/6731 ratio is an useful measure of density (increasing from top to bottom).

riety of new facts. The emitting gas is highly differentiated in its kinematic properties: the hydrogen-emitting and forbidden-line-emitting gas have in general similar motion, but may also sometimes show highly contrasting velocities, as in the case of the Tr 14 shell. The low-level high-velocity emission was studied here with better detail than in previous studies, thanks to the very large S/N of the new data.

We have presented new evidence showing that the wide  $H\alpha$  wings arise from reflection of the emission of  $\eta$  Car off dust, strengthening results from previous works. However, to be entirely consistent with our observations, such dust cannot be stationary, but expanding away from  $\eta$  Car. It should be remarked that  $\eta$  Car is spectrally variable on timescales shorter than the light-crossing time ( $\sim 11$  yr) of the putative dust shell radius of  $\sim 5$  arcmin. Regarding longer-term variability, we are fortunate that such a 11-yr delay between the direct and reflected  $\eta$  Car emission coincides nearly with the time difference between our observational data sets (2002-2004 for  $\eta$  Car UVES spectra; Apr. 2014 for the bulk of our HR15N nebular spectra): this makes that the comparison between  $\eta$  Car and its reflected emission, e.g. in Fig. 21, is unaffected by long-term variations.

The narrow excess emission seen in the  $H\alpha$  fit residuals between absolute RVs of 50-100 km/s is of uncertain significance. More significant is instead the occasional excess emission in the [S II] lines, in the same RV range. Such enhanced high-velocity [S II] emission appears at almost random places; it might be originated where the fast OB star winds encounter local overdensities in the ambient medium, with formation of shocks, as suggested by line-ratio diagrams. The reason why this phenomenon happens preferentially around  $|RV| \sim 100$  km/s is also unclear; it might be only a coincidence that this is close to the sound speed in the million-degree hot plasma which is found diffusely in the same region (Townsley et al. 2011), and which is supposed to be

also heated by shocks caused by the OB stars winds. A detailed theoretical investigation of the complex observed phenomena in this complex region would be certainly desirable.

The two main expanding layers at  $RV \sim RV_{cm} \pm 20$  km/s were known long before this work, as mentioned in the introduction. The  $\sim 20' \times 20'$  spatial region studied here, in the brightest, central part of Carina, is nearly the same as that studied by Deharveng and Maucherat (1975) using lesser-quality data, and covers about one-third of that studied by Meaburn, Lopez and Keir (1984), who however analyzed Fabry-Perot spectra only along two lines crossing Carina. Our findings from the previous section support a local origin for the bulk of approaching/receding line emission, from few discrete expanding shells of gas surrounding the most massive stars. In order to place these findings in the appropriate context, we may refer to the larger-scale images in Smith and Brooks (2007), and their Figure 5b in particular, showing an  $H\alpha/[O III]$  flux-ratio image. This figure suggests strongly that the entire Carina nebula is composed by a collection of shells and cavities, of projected sizes in the range 15-60 arcmin, and thus much larger than the shells found in this work. Both Trumpler 14 and 16 are found in the northern lobe of a bipolar cavity (see also Smith et al. 2000), apparently split in two by the dark dust lanes. The same image does not show subshells of smaller scale, corresponding to those we have described in the previous section (all falling in the same northern lobe of the bipolar cavity). To reconcile our results with the larger-scale gas bubbles, we hypothesize that our shells have already started to merge together, producing the larger structures of the bipolar cavity. This structure, with each of its lobes having an asymmetrical shape, must also have a very complex velocity field, according to the remark by Meaburn, Lopez and Keir (1984) that a spherically expanding nebula would not fit their dynamical data. Our data do not show any velocity component clearly associated to the post-merging expansion: the velocity of this latter might be close to the dominant shell approaching/receding velocity, or very different but undetected because of the much lower intensity of its emission (which might have remained hidden within the complex fit residuals shown in Fig. 17).

Another important result from the data presented is the existence of significant gradients, typically with plane-parallel geometries rather than spherical geometries. Also the mentioned “shells” develop along preferred directions, rather than along a radial direction: they should better termed “cylinders”, although the physical mechanism leading to this type of expansion geometry is not easy to understand. Nitrogen ionization fraction also shows significant gradients: in the  $\eta$  Car shell these are explained by a polar-angle dependence of the ionizing flux incident on the Nebula. In general, two preferred directions appear to be those of the two obscuring dust lanes. In addition to this dark material, also other layers of “invisible” material were shown to exist: one example is the massive (neutral?) layer moving at  $RV \sim -10$  km/s against which part of the Tr 14 shell appears to have collided; another example is the neutral material moving at  $RV \sim -100$  to 0 km/s, causing the known interstellar absorption lines towards Carina stars. The complexity of observed structures in the studied region is such that there are no truly representative “average” conditions, holding to a good approximation everywhere in the region: in order to put other studies (like e.g. on the stellar populations of clusters Tr 14 and 16) into a proper context, a careful consideration of local conditions is highly needed.

## 5. Summary

We have studied the profiles of optical emission lines of  $H\alpha$ , [N II], [S II] and He I on more than 650 sightlines in the central part of the Carina Nebula. We recover the known double-peaked line profiles in all lines, and through gaussian fits to the lines we show that also single-peaked lines actually arise from two distinct components, from approaching and receding gas. The main properties of the gas yielding the bulk nebular emission are the following:

- The motion of gas in the central  $20' \times 20'$  of the Carina Nebula indicates the existence of several distinct expanding shells, centered on  $\eta$  Car, Tr 14, WR25, and possibly the O3 star HD93250.
- The shape of these shells is non-spherical, with preferential directions for expansion that are related to the geometry of the dark obscuring dust lanes, and abrupt distortions likely caused by collisions with higher-density material; traces of collisions between adjacent shells are also found.
- $H\alpha$  emitting gas is basically the same as He I emitting gas, while significant kinematical differences are found with respect to gas emitting in the forbidden lines.
- The gas temperature is found to be  $\sim 10^4$  K from line-width ratios of H and He, and slightly hotter in the approaching component.
- Gas densities were derived from the [S II] doublet ratio, and found in the range  $200\text{--}300 \text{ cm}^{-3}$ , increasing towards the inner parts of the Nebula, and near inter-shell boundaries.
- The N ionization fraction is found to increase systematically towards the South in the approaching component, with an almost opposite trend for the receding component. In the  $\eta$  Car shell, this varying ionization is shown to be correlated with angular distance from the Homunculus polar axis.
- Within a small sample of sky directions, the differential Balmer decrement between approaching and receding gas indicates a very low extinction. Therefore, dust causing the occasionally large measured extinction must be located either in front or behind the shells observed in  $H\alpha$  (and stars contained within them) but not inside the shells.
- The shell sizes and expansion velocities imply short timescales of  $\sim 1.5 \cdot 10^5$  years for the ionized gas.

We also found significant residual emission at large absolute RVs, after subtracting out the main gaussian components from the observed profiles. A wide component is very often found in  $H\alpha$ , while narrow components are occasionally found in [S II], and with less confidence in  $H\alpha$  as well. We have found several distinct pieces of evidence that such wide  $H\alpha$  wings arise from reflection of the  $\eta$  Car spectrum (in agreement with previous studies), and that the reflecting dust is likely radially expanding to account for the observed asymmetry in these wings. Reflection nebulosity is also indicated by the level of sky continuum in places other than the Keyhole, notably near the Tr 14 core. The [S II] narrow components are instead suggestive of localized shocks, as also hypothesized for the diffuse X-ray emission already known in the region.

We remark that the observational data presented here were not originally taken with the purpose of studying the nebular emission: according to the Gaia-ESO Survey observing strategy, a number of fibres is routinely targeted at empty sky positions, in order to eliminate the sky contribution from the stellar spectra. This study demonstrates the rich scientific content of Gaia-ESO Survey data, even surpassing their intended objectives.

**Acknowledgements.** We wish to thank an anonymous referee for his/her helpful suggestions. Based on data products from observations made with ESO Telescopes at the La Silla Paranal Observatory under programme ID 188.B-3002. These data products have been processed by the Cambridge Astronomy Survey Unit (CASU) at the Institute of Astronomy, University of Cambridge, and by the FLAMES/UVES reduction team at INAF/Osservatorio Astrofisico di Arcetri. These data have been obtained from the Gaia-ESO Survey Data Archive, prepared and hosted by the Wide Field Astronomy Unit, Institute for Astronomy, University of Edinburgh, which is funded by the UK Science and Technology Facilities Council. This work was partly supported by the European Union FP7 programme through ERC grant number 320360 and by the Leverhulme Trust through grant RPG-2012-541. We acknowledge the support from INAF and Ministero dell’ Istruzione, dell’ Università’ e della Ricerca (MIUR) in the form of the grant "Premiale VLT 2012". The results presented here benefit from discussions held during the Gaia-ESO workshops and conferences supported by the ESF (European Science Foundation) through the GREAT Research Network Programme. This research has made use of the SIMBAD database, operated at CDS, Strasbourg, France.

## References

- Albacete-Colombo, J. F., Damiani, F., Micela, G., Sciortino, S., & Harnden, F. R., Jr. 2008, *A&A*, 490, 1055
- Boumis, P., Meaburn, J., Bryce, M., & Lopez, J. A. 1998, *MNRAS*, 294, 61
- Cohen, M., & Kuhi, L. V. 1979, *ApJS*, 41, 743
- Davidson, K., & Humphreys, R. M. 1997, *ARA&A*, 35, 1
- Davidson, K., Smith, N., Gull, T. R., Ishibashi, K., & Hillier, D. J. 2001, *AJ*, 121, 1569
- Deharveng, L., & Maucherat, M. 1975, *A&A*, 41, 27
- Gilmore, G., Randich, S., Asplund, M., et al. 2012, *The Messenger*, 147, 25
- Haffner, L. M., Dettmar, R.-J., Beckman, J. E., et al. 2009, *Reviews of Modern Physics*, 81, 969
- Hartigan, P., Morse, J. A., Tumlinson, J., Raymond, J., & Heathcote, S. 1999, *ApJ*, 512, 901
- Krumholz, M. R., & Burkhardt, B. 2015, arXiv:1512.03439
- Lopez, J. A., & Meaburn, J. 1984, *Rev. Mexicana Astron. Astrofis.*, 9, 119
- Meaburn, J., Lopez, J. A., & Keir, D. 1984, *MNRAS*, 211, 267
- Osterbrock, D. E., & Ferland, G. J. 2006, *Astrophysics of gaseous nebulae and active galactic nuclei*, 2nd. ed. by D.E. Osterbrock and G.J. Ferland. Sausalito, CA: University Science Books, 2006
- Pasquini, L., Avila, G., Blecha, A., et al. 2002, *The Messenger*, 110, 1
- Povich, M. S., Smith, N., Majewski, S. R., et al. 2011, *ApJS*, 194, 14
- Randich, S., Gilmore, G., & Gaia-ESO Consortium 2013, *The Messenger*, 154, 47
- Riesgo, H., & López, J. A. 2006, *Rev. Mexicana Astron. Astrofis.*, 42, 47
- Sabbadin, F., Minello, S., & Bianchini, A. 1977, *A&A*, 60, 147
- Seward, F. D., Forman, W. R., Giacconi, R., et al. 1979, *ApJ*, 234, L55
- Smith, N., Egan, M. P., Carey, S., et al. 2000, *ApJ*, 532, L145
- Smith, N., Bally, J., & Brooks, K. J. 2004, *AJ*, 127, 2793
- Smith, N., Stassun, K. G., & Bally, J. 2005, *AJ*, 129, 888
- Smith, N. 2006, *ApJ*, 644, 1151
- Smith, N., & Brooks, K. J. 2007, *MNRAS*, 379, 1279
- Smith, N., & Brooks, K. J. 2008, *Handbook of Star Forming Regions*, Volume II, 138
- Townsend, L. K., Broos, P. S., Chu, Y.-H., et al. 2011, *ApJS*, 194, 15
- Viironen, K., Delgado-Inglada, G., Mampaso, A., Magrini, L., & Corradi, R. L. M. 2007, *MNRAS*, 381, 1719
- Walborn, N. R. 1973, *ApJ*, 179, 517
- Walborn, N. R., & Hesser, J. E. 1975, *ApJ*, 199, 535
- Walborn, N. R., & Liller, M. H. 1977, *ApJ*, 211, 181
- Walborn, N. R., Danks, A. C., Vieira, G., & Landsman, W. B. 2002, *ApJS*, 140, 407
- Walborn, N. R., Smith, N., Howarth, I. D., et al. 2007, *PASP*, 119, 156
- Wilson, R. E. 1953, *Carnegie Institute Washington D.C. Publication*
- Wolk, S. J., Broos, P. S., Getman, K. V., et al. 2011, *ApJS*, 194, 12
- Yonekura, Y., Asayama, S., Kimura, K., et al. 2005, *ApJ*, 634, 476



**Table 1.** Double-gaussian fitting results for H $\alpha$ . Full table available electronically.

Nr.	Id	Type/setup	RA	Dec	H $\alpha$					
			(J2000)	(J2000)	Norm <sub>blue</sub>	RV <sub>blue</sub>	$\sigma_{blue}$	Norm <sub>red</sub>	RV <sub>red</sub>	$\sigma_{red}$
1	SKY__10434580-5930497	sky_HR15N	160.94083	-59.51381	43435.14	-23.61	15.61	58918.77	4.94	13.38
2	SKY__10445840-5933062	sky_HR15N	161.24333	-59.55172	18256.59	-31.12	13.93	34321.84	5.23	15.21
3	SKY__10445040-5935467	sky_HR15N	161.21000	-59.59631	34377.49	-28.47	13.77	65136.86	-0.09	17.20
4	SKY__10443390-5934549	sky_HR15N	161.14125	-59.58192	34307.92	-29.53	14.51	30563.08	-15.04	23.81
5	SKY__10451730-5942205	sky_HR15N	161.32208	-59.70569	37527.72	-28.25	15.50	22025.68	14.37	14.07
6	SKY__10451970-5945404	sky_HR15N	161.33208	-59.76122	24245.06	-21.95	15.87	9017.24	11.42	15.95
7	SKY__10444430-5943333	sky_HR15N	161.18458	-59.72592	30519.80	-34.15	14.82	53892.78	7.00	14.64
8	SKY__10440670-5947505	sky_HR15N	161.02792	-59.79736	8057.94	-24.88	16.14	10603.72	10.00	15.99
9	SKY__10441789-5948152	sky_HR15N	161.07458	-59.80422	6677.84	-21.83	17.05	5186.23	6.33	17.29
10	SKY__10441380-5943572	sky_HR15N	161.05750	-59.73256	20338.31	-28.54	15.25	32785.90	2.83	16.33
11	SKY__10435880-5944037	sky_HR15N	160.99500	-59.73436	10317.80	-29.29	13.93	37845.24	2.46	16.48
12	SKY__10434210-5933208	sky_HR15N	160.92542	-59.55578	57426.48	-13.00	21.76	44337.46	-0.38	14.19
13	SKY__10434580-5930497	sky_HR15N	160.94083	-59.51381	42161.66	-24.58	15.38	65908.87	4.63	13.99
14	SKY__10452410-5932317	sky_HR15N	161.35042	-59.54214	9307.17	-37.75	15.04	29908.25	3.90	17.32
15	SKY__10451230-5939301	sky_HR15N	161.30125	-59.65836	57393.14	-32.90	14.24	46170.07	14.59	14.92
16	SKY__10454120-5937395	sky_HR15N	161.42167	-59.62764	25817.26	-29.33	18.31	44071.29	6.19	14.04
17	SKY__10451730-5942205	sky_HR15N	161.32208	-59.70569	42171.85	-28.09	15.39	24532.33	14.49	13.80
18	SKY__10451270-5940065	sky_HR15N	161.30292	-59.66847	43023.05	-35.24	14.52	120581.13	6.87	14.57
19	SKY__10452060-5943215	sky_HR15N	161.33583	-59.72264	58355.08	-25.32	16.09	24757.19	16.24	12.64
20	SKY__10451970-5945404	sky_HR15N	161.33208	-59.76122	24230.63	-22.13	15.46	10209.32	10.43	16.47
21	SKY__10451060-5946127	sky_HR15N	161.29417	-59.77019	32485.39	-22.23	15.18	10906.66	13.17	16.08
22	SKY__10444180-5944315	sky_HR15N	161.17417	-59.74208	36492.25	-32.92	15.70	62097.00	8.54	14.32
23	SKY__10445440-5941005	sky_HR15N	161.22667	-59.68347	62865.35	-34.23	14.74	38519.34	7.42	16.72
24	SKY__10435880-5944037	sky_HR15N	160.99500	-59.73436	9487.00	-27.55	14.85	29200.92	3.55	16.34
25	SKY__10441810-5941175	sky_HR15N	161.07542	-59.68819	76112.44	-29.23	14.03	135383.63	4.77	14.46

**Table 2.** Double-gaussian fitting results for [N II] 6584 and He I 6678. Full table available electronically.

Nr.	[N II] 6584						He I 6678					
	Norm <sub>blue</sub>	RV <sub>blue</sub>	$\sigma_{blue}$	Norm <sub>red</sub>	RV <sub>red</sub>	$\sigma_{red}$	Norm <sub>blue</sub>	RV <sub>blue</sub>	$\sigma_{blue}$	Norm <sub>red</sub>	RV <sub>red</sub>	$\sigma_{red}$
1	2943.68	-31.66	14.71	11672.97	2.10	10.67	15235.06	-22.16	13.79	18024.73	5.19	10.38
2	1130.41	-24.70	15.34	4429.57	5.90	15.36	5555.79	-30.83	11.55	11833.37	5.01	13.96
3	2528.38	-22.84	13.49	3541.20	9.64	14.93	11447.99	-28.24	10.67	22875.81	0.41	14.87
4	10198.94	-25.17	12.26	3538.75	-12.05	25.62	10756.85	-29.39	12.29	11023.40	-15.58	23.19
5	6328.36	-28.63	13.16	2644.65	15.04	12.74	9441.61	-27.95	11.69	7676.87	13.18	13.84
6	4011.71	-17.86	13.23	2122.03	-7.92	27.32	7065.39	-17.61	13.23	1828.86	14.34	8.58
7	7207.63	-33.96	12.22	5305.92	9.02	13.03	9951.92	-32.18	14.02	17619.99	7.92	12.14
8	1587.50	-20.77	13.62	937.43	11.35	15.09	1064.69	-31.31	8.00	4338.92	5.87	17.68
9	1703.78	-6.20	21.61	525.83	-19.22	10.75	2466.90	-10.28	18.70	266.07	16.04	6.46
10	1684.90	-13.38	11.60	5422.81	-7.82	21.49	5930.21	-30.20	11.87	10660.00	2.94	13.60
11	4373.97	-3.49	19.85	830.40	-21.12	10.20	2127.89	-33.45	8.29	12921.66	1.03	13.87
12	4685.66	-33.46	14.92	6965.35	0.05	12.48	22855.47	-8.70	18.91	10122.84	0.02	10.93
13	2800.86	-33.03	14.29	13198.67	2.00	11.49	12023.08	-26.25	12.42	23322.05	4.31	12.59
14	2186.93	-16.49	17.16	3758.53	14.88	11.74	3443.08	-32.95	15.86	7619.56	4.88	14.10
15	3167.91	-31.88	13.19	5243.57	12.54	13.00	19613.70	-32.19	11.88	15360.44	16.24	12.72
16	3011.29	-30.13	18.32	8014.10	6.37	11.96	5516.82	-33.65	14.53	16154.50	4.63	13.21
17	7134.41	-28.55	13.13	3000.12	15.01	12.16	13148.70	-28.02	12.73	8012.74	14.22	12.18
18	2994.32	-29.87	14.65	12788.21	8.36	12.14	13590.73	-35.56	11.32	43233.80	6.74	12.91
19	12502.16	-26.42	12.22	3405.79	15.45	10.99	16662.09	-24.51	12.98	8898.32	16.20	11.20
20	3188.13	-20.08	11.56	3135.33	-5.20	22.15	6146.43	-22.07	12.88	3727.43	11.31	15.12
21	8912.84	-21.74	12.62	1470.43	16.12	13.00	7698.10	-22.79	12.53	3627.53	11.56	15.87
22	6138.80	-29.72	12.10	4917.66	12.05	12.53	9370.82	-33.21	13.37	22366.58	9.27	12.79
23	3765.67	-24.34	19.62	4338.87	9.45	13.73	21464.20	-33.51	12.20	12253.55	8.20	15.55
24	526.71	-21.23	9.50	3724.93	-3.80	20.34	3277.37	-24.19	11.73	9583.29	4.69	13.13
25	11314.24	-21.00	17.92	9176.47	8.85	12.04	25493.19	-29.10	11.79	46905.75	4.43	12.16

## Appendix A: On the Giraffe/HR15N instrumental line profile

In section 3.2 we have examined best-fit residuals with amplitudes of 1-2% with respect to peak emission. Our ability to draw meaningful conclusions from such low-level features (in relative terms) in our data requires some detailed understanding of the instrumental response. We have therefore examined Th-Ar calibration lamp spectra, nearly simultaneous to some of the data studied here. These spectra are crowded of lines, and therefore only very few lines were isolated and bright enough for a study of their extreme tails down to less than 1% of peak. One such example is shown in Figure A.1, where the abscissa  $\Delta\lambda$  is transformed into a velocity scale to facilitate comparison with results in section 3.2. In the same Figure we show one-gaussian (red) and two-gaussian (blue) best-fit models to the lamp line profile, and their residuals. The one-gaussian model is discrepant from the observed line profile at a level of 3-4% maximum. The two-gaussian model residuals are much smaller, slightly exceeding 1% discrepancy. The profile obtained by convolving the lamp profile with a gaussian with  $\sigma = 10$  km/s (e.g., a typical turbulent or thermal width), however, yields residuals of only 1% when fitted with only one gaussian. At face value, this would suggest that by approximating the instrumental spectral response with a simple gaussian we should expect spurious fit residuals of order of 1% of peak emission. However, in Figure 17 we may observe that the oscillating residuals around zero velocity often exceed the 1% level (indicated by the horizontal dashed lines), and show a typical peak-to-peak RV interval of  $\sim 30 - 40$  km/s, while the residual oscillations in Fig. A.1 occur at the 1-2 pixel level (RV intervals  $\sim 4 - 8$  km/s). The latter property especially would indicate that the nebular fit residuals are unrelated to non-gaussianity of the instrumental line profile.

To clarify the problem more accurately, we have considered the above two-gaussian model for the lamp line profile as the basis for our nebular-line fitting procedure. The normalized lamp line profile was modeled using two gaussians as:

$$\lambda(v) = \frac{A_1}{\sqrt{2\pi\sigma_1^2}} \exp\left(-\frac{(v-v_1)^2}{2\sigma_1^2}\right) + \frac{A_2}{\sqrt{2\pi\sigma_2^2}} \exp\left(-\frac{(v-v_2)^2}{2\sigma_2^2}\right) \quad (\text{A.1})$$

with best-fit parameter values:  $v_1 = -6.404371$  km/s,  $\sigma_1 = 6.44256$  km/s,  $A_1 = 0.3966431$ ,  $v_2 = 3.454723$  km/s,  $\sigma_2 = 6.069641$  km/s, and  $A_2 = 0.6033569$ .

The convolution of  $\lambda(v)$  with a gaussian was then used in place of a simple gaussian, as the basic ingredient of our two-component nebular-line fits, as in section 3.1. The fit residuals were then computed as in section 3.2. In this way we obtained residual patterns almost indistinguishable from those shown in Fig. 17. We conclude that all systematic peculiarities found in those residuals, and discussed in section 3.2, do not arise because of instrumental effects, but reflect actual properties of the nebular lines.

**Table 3.** Double-gaussian fitting results for [S II] 6717 and 6731. Full table available electronically. Parameters are not given when the fit did not converge.

Nr.	[S II] 6717						[S II] 6731					
	Norm <sub>blue</sub>	RV <sub>blue</sub>	$\sigma_{blue}$	Norm <sub>red</sub>	RV <sub>red</sub>	$\sigma_{red}$	Norm <sub>blue</sub>	RV <sub>blue</sub>	$\sigma_{blue}$	Norm <sub>red</sub>	RV <sub>red</sub>	$\sigma_{red}$
1	998.76	-32.45	12.98	3398.53	4.20	10.39	727.14	-33.94	12.95	2696.04	3.09	10.02
2	1655.72	-4.40	19.00	736.73	9.41	9.97	1304.64	-4.45	19.94	519.97	8.08	9.21
3	1733.36	-20.27	18.14	950.03	14.14	12.06	1352.34	-19.90	18.25	642.85	13.89	11.27
4	2687.79	-21.74	12.12	740.18	7.11	32.20	2636.84	-22.17	11.68	582.76	6.44	32.56
5	1748.67	-25.49	12.72	836.83	16.73	11.97	1313.25	-26.18	12.99	610.61	16.64	11.96
6												
7	2213.11	-31.97	11.54	1278.25	10.42	13.44	1662.81	-32.62	11.37	933.80	9.52	13.01
8												
9												
10												
11	469.30	-18.53	9.54	1110.19	-0.66	20.34	366.52	-17.40	10.31	866.86	-2.12	21.39
12												
13	967.95	-32.94	12.99	3802.68	4.36	11.14	691.68	-33.68	12.85	3033.48	3.42	10.71
14	667.02	-14.19	14.92	1498.09	16.50	11.59	448.63	-17.26	13.95	1137.60	15.03	11.83
15	1093.46	-28.97	11.44	1380.37	12.65	13.00	791.13	-29.16	11.26	1049.22	11.93	12.59
16	1528.20	-26.27	20.60	1249.28	10.53	10.68	1076.97	-26.00	20.08	991.71	9.75	10.83
17	1988.85	-25.27	13.06	960.64	17.27	11.89	1437.02	-25.62	12.76	687.35	16.37	11.25
18	1013.07	-27.23	13.68	2715.95	10.73	11.64	724.03	-27.75	13.29	2280.19	9.77	11.25
19	4184.69	-24.85	11.55	926.70	17.31	10.44	3029.70	-25.83	11.14	699.69	15.96	10.98
20												
21												
22	3028.96	-27.92	10.67	1108.90	14.41	12.80	2149.86	-28.79	10.36	851.78	13.11	12.83
23												
24												
25	2519.56	-30.03	15.18	2615.40	9.17	12.48	1890.12	-30.80	15.31	2041.98	8.08	11.98

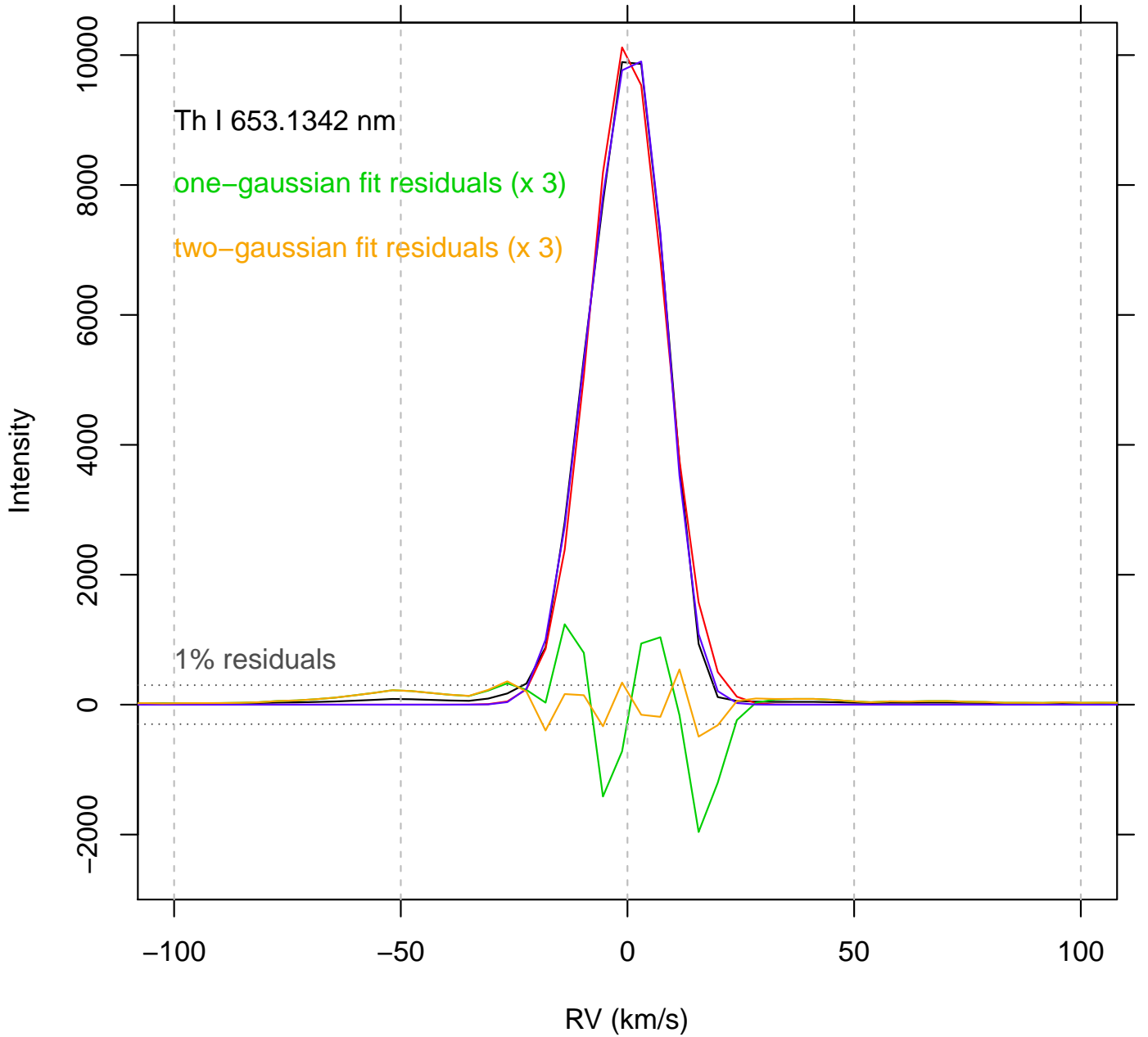


**Fig. A.1.** Giraffe HR15N Th-Ar lamp line (black), and best-fit one-gaussian (red) and two-gaussian (blue) models. To facilitate comparison with earlier results the abscissa is shown on a velocity scale. Best-fit residuals, scaled-up three times, are shown in green and orange for the one- and two-gaussian models, respectively. The vertical dashed grey lines correspond to those shown in Figure 17; the horizontal dotted lines indicate amplitudes in the residuals of  $\pm 1\%$  of peak, like the horizontal lines in Fig. 17.